μSR STUDIES OF THE ELECTRON-DOPED HIGH-T_C SUPERCONDUCTOR $Pr_{2-X}Ce_XCuO_4$

by

Ka Fai Poon

B. Sc., McGill University, 1999

THESIS SUBMITTED IN PARTIAL FULFILLMENT

OF THE REQUIREMENTS FOR THE DEGREE OF

MASTER OF SCIENCE

IN THE DEPARTMENT

OF

PHYSICS

© Ka Fai Poon 2003

SIMON FRASER UNIVERSITY

May 2003

All rights reserved. This work may not be
reproduced in whole or in part, by photocopy
or other means, without permission of the author.

APPROVAL

Name: Ka Fai Poon

Degree: Master of Science

Title of Thesis: μSR Studies of the electron-doped high-T_c superconductor $Pr_{2-x}Ce_xCuO_4$

Examining Committee: Dr. H. D. Trottier (Chair)

Dr. J. E. Sonier, Senior Supervisor
Assistant Professor, Department of Physics

Dr. J. S. Dodge,
Assistant Professor, Department of Physics

Dr. M. E. Hayden,
Assistant Professor, Department of Physics

Dr. D. B. Leznoff, Internal Examiner
Assistant Professor, Department of Chemistry

Date Approved: May 15, 2003

Abstract

This thesis reports muon-spin rotation/relaxation (μSR) measurements on single crystals of the electron-doped high-T_c superconductor $Pr_{2-x}Ce_xCuO_4$. In zero external magnetic field, superconductivity is found to coexist with slowly fluctuating Cu spins that are randomly oriented. We do not observe any magnetic order at temperatures above 2.3 K. However, in an applied field, the resultant magnetic field at the muon stopping site is increased upon cooling the sample below the superconducting transition temperature, T_c. This implies the onset of an additional source of static magnetic order throughout the sample. From dipolar-field calculations we have determined that this is consistent with vortex-induced antiferromagnetic (AF) ordering of the Cu spins. In addition, we have carried out the first measurements of the in-plane magnetic penetration depth λ_{ab} in the vortex state of $Pr_{2-x}Ce_xCuO_4$ single crystals. We find that the temperature dependence of λ_{ab} resembles that of the hole-doped cuprates at temperatures above $\sim 0.2\ T_c$. However, due to the small size of the single crystals it was not possible to determine the limiting low-temperature behaviour of λ_{ab}.

Acknowledgments

First I would like to thank Jeff Sonier for his patience and excellent supervision on this thesis. His support in helping me navigate through the intricate physics greatly enhance my learning experience. I am grateful for the insightful comments from Jess Brewer on this thesis. I thank the following people for their assistance in setting up and running this experiment: Robert Kiefl, Graeme Luke, Patrick Kyriakou, Roger Miller, Chris Wiebe, Scott Stubbs and the TRIUMF technical staff: including Donald Arseneau, Bassam Hitti and Syd Kreitzman. I thank Richard Greene and Patrick Fournier for providing the single crystals which made this experiment possible. Special thanks to Ruixing Liang for his assistance with the magnetization measurements.

Contents

Approval **ii**

Abstract **iii**

Acknowledgments **iv**

Contents **v**

List of Figures **vii**

1 Introduction **1**

2 μSR Spectroscopy **5**

2.1 Introduction 5

2.2 Time Differential μSR (TD-μSR) 7

2.3 Transverse-Field μSR (TF-μSR) 10

2.4 Fast Fourier Transform (FFT) 13

2.5 Zero-Field μSR (ZF-μSR) 14

3 Experimental Details **18**

3.1 Crystal Growth Process 18
3.2 Sample Characteristics 19
3.3 Experimental Setup 21

4 Zero-Field Measurements **24**

5 Transverse-Field Measurements **30**

6 Discussion **47**

Bibliography **52**

List of Figures

1.1 Generic Phase diagram of the hole-doped HTSC $La_{2-x}Sr_xCuO_4$ and the electron-doped HTSC $Pr_{2-x}Ce_xCuO_4$ as a function of charge doping concentration 2

2.1 Angular distribution of positrons from μ^+ decay with respect to the initial muon spin direction 8

2.2 Schematic diagram for a typical TD-μSR experiment 9

2.3 Schematic diagram of a TF-μSR experiment 11

2.4 Schematic diagram of a ZF-μSR experiment 15

3.1 Crystal structure of $La_{2-x}Sr_xCuO_4$ and $Pr_{2-x}Ce_xCuO_4$ 20

3.2 Bulk magnetic susceptibility measurements taken under FC and ZFC conditions with H = 1 Oe and resistivity measurements in zero external magnetic field 22

3.3 Schematic of the experimental setup 22

4.1 Time evolution of the asymmetry in zero external magnetic field at T = 165 K, 80 K, 40 K and 2.3 K. 25

4.2 Time evolution of the asymmetry in longitudinal external magnetic fields of 100 Oe and 25 Oe, at T = 25 K. 26

4.3 Temperature dependence of the amplitudes a_1 and a_2 28

4.4 Temperature dependence of the relaxation rates Δ and λ. 29

5.1 Time evolution of the muon-spin polarization in $Pr_{2-x}Ce_xCuO_4$ taken under (a) FC and (b) ZFC conditions at T = 2.4 K 31

5.2 Time evolution of the muon-spin polarization in $Pr_{2-x}Ce_xCuO_4$ taken under (a) FC and (b) ZFC conditions at H = 91 Oe 32

5.3 FFTs of the muon-spin precession signal in $Pr_{2-x}Ce_xCuO_4$ 33

5.4 Temperature dependence of $B_0 - \mu_0 H$ at H = 91, 200, 500 and 2019 Oe
Inset: Magnetic field dependence of $B_0 - \mu_0 H$ at T = 5 and 25 K 35

5.5 $K^{\perp}$ vs. $\chi^{\perp}$ at H = 3 kOe.
Inset: Temperature dependence of $\chi^{\perp}$ and $\chi^{\parallel}$ at H = 10 kOe. 36

5.6 Temperature dependence B_0 and $\chi^{\perp}$ measured under FC conditions at H = 91 and 500 Oe 38

5.7 Magnetic field dependence of B_0^S - B_0^N at T = 5 K and 10 K 39

5.8 Top: Two proposed ordered Cu-spin structures for Pr_2CuO_4
Bottom: Magnetic field strength at the muon stopping site due to Cu dipole moments plotted as a function of the canting angle θ between the Cu spins and the CuO_2 plane 41

5.9 FFTs of the muon-spin precession signal and the theoretical muon-spin polarization functions with $G(t) = e^{-(\Delta t)^{\beta}}$ where β = 1.2, and $G(t) = e^{-(\sigma^2 t^2)/2}$ 42

5.10 Temperature dependence of λ_{ab} for a $Pr_{2-x}Ce_xCuO_4$ single crystal with ξ_{ab} = 30 Å and 60 Å at H = 91 Oe 43

5.11 Temperature dependence of the magnetic penetration depth $\lambda_{ab}^{-2}(T)$ at H = 91 Oe 44

5.12 Temperature dependence of the magnetic penetration depth in a second $Pr_{2-x}Ce_xCuO_4$ single crystal at H = 200 Oe 46

5.13 Normalized magnetic penetration depth $\lambda_{ab}^2(0)/\lambda_{ab}^2(T)$ as a function of reduced temperature T/T_c for $Pr_{2-x}Ce_xCuO_4$ single crystals at H = 91 Oe, $La_{2-x}Sr_xCuO_4$ at H = 2 kOe and $YBa_2Cu_3O_{6.95}$ at H = 5 kOe 46

Chapter 1

Introduction

In 1986, Bednorz and Müller discovered superconductivity in the $La_{2-x}Ba_xCuO_{4+y}$ system, below a critical transition temperature $T_c \approx 30$ K [1]. This finding was subsequently followed by the discovery of high-T_c superconductivity in a number of related layered compounds consisting of CuO_2 planes. The CuO_2 planes in these materials are separated by "charge reservoir layers", which control the oxidation state of the copper ions. High-T_c superconductivity is achieved when the undoped parent compound (*e.g.* La_2CuO_4), which is an antiferromagnetic insulator, is doped with *holes* (Fig. 1.1) [2]. An exception is the $R_{2-x}Ce_xCuO_4$ system, where R = {La, Nd, Pr, Sm or Eu}. In this case, high-T_c superconductivity occurs upon partial substitution of Ce^{4+} for R^{3+}, which dopes *electrons* into the CuO_2 layers. The most studied electron-doped high-T_c superconductor (HTSC) is $Nd_{2-x}Ce_xCuO_4$, which was synthesized by Tokura and co-workers in 1989 [3]. Compared to hole-doped HTSC's, less is known about the electron-doped cuprates. One reason is that it is difficult to synthesize high-quality single crystals. In contrast to the hole-doped compounds, as-grown crystals are made superconducting by subjecting them to an oxygen reduction process [4], which often degrades the crystal surface. In addition, single crystals

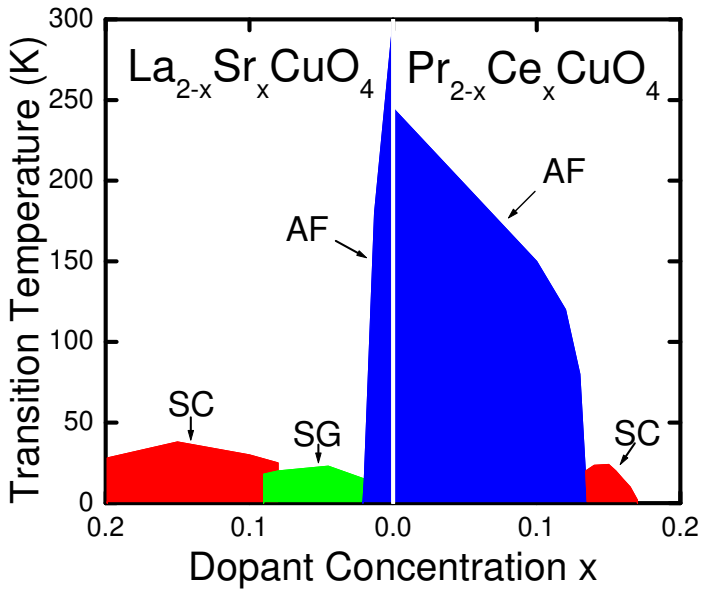

Fig. 1.1: Generic Phase diagram of the hole-doped HTSC $La_{2-x}Sr_xCuO_4$ and the electron-doped HTSC $Pr_{2-x}Ce_xCuO_4$ as a function of charge doping concentration, showing the anitferromagnetic (AF), spin glass (SG) and superconducting (SC) phases.

of electron-doped cuprates are generally plagued by spatial inhomogeneity of the cerium and oxygen concentration [5, 6].

One of the fundamental properties of superconductors is that they exhibit a diamagnetic response called the "Meissner effect." When a superconducting material is cooled below T_c in the presence of a weak applied magnetic field H, the field is expelled from the bulk of the sample. When the applied magnetic field exceeds a critical value H_c, superconductivity is destroyed. For type-II superconductors, like the high-T_c cuprates, the response to an applied

magnetic field can be one of the following:

1. **Meissner State**: At $H < H_{c1}$, (where $H_{c1} \equiv$ the lower critical magnetic field), supercurrents circulate near the surface of the sample, screening the magnetic field from the bulk. However, the external magnetic field partially penetrates the sample at the surface. The magnitude of the penetrating field-component parallel to the surface decays exponentially [7] as a function of distance from the surface. The characteristic length scale of the exponential field decay is the "magnetic penetration depth" λ. This quantity is of fundamental importance, as λ^{-2} is proportional to the density of superconducting carriers n_s.

2. **Vortex State**: At $H_{c1} < H < H_{c2}$ (where $H_{c2} \equiv$ the upper critical magnetic field), magnetic flux penetrates the bulk of the superconductor in the form of a periodic arrangement of quantized flux lines, called a "vortex lattice". Each vortex in the lattice is comprised of one flux quantum $\Phi = hc/2e$. The vortex core is a region where the "superconducting order parameter" $\psi(r)$ is suppressed and the local magnetic field $B(r)$ is maximum (r is the radial distance from the centre of the vortex). The length scale which governs spatial variations of $\psi(r)$ is called the "superconducting coherence length" ξ. Supercurrents circulating around the individual vortices screen the magnetic field within the vortex core from the surrounding material, in the same way that supercurrents near the sample surface screen the external magnetic field in the Meissner state. Consequently, the magnetic field decays outside the vortex core region over the length scale λ.

3. **Normal State**: $H > H_{c2}$, the external magnetic field fully penetrates the sample and superconductivity is destroyed.

One of the outstanding issues concerning the electron-doped HTSCs is the pairing symmetry of the superconducting carriers in these compounds. While there are phase sensitive [8], angle resolved photoemission spectroscopy [9] and microwave [10] measurements that suggest the pairing symmetry is $d_{x^2-y^2}$-wave (like in hole-doped HTSCs), other experiments [11, 12] favour *s*-wave symmetry. Measurements of the temperature dependence of the magnetic penetration depth are one way of distinguishing between *s*-wave and $d_{x^2-y^2}$-wave symmetry. Thus far, most measurements of λ in electron-doped HTSCs have been performed in the Meissner state. In this thesis, the results of measurements of the in-plane magnetic penetration depth λ_{ab} in the vortex state of the electron-doped HTSC $Pr_{2-x}Ce_xCuO_4$, by muon spin rotation (μSR) spectroscopy are presented. As a bulk local probe, μSR has the advantage that it is insensitive to inhomogeneities at the sample surface. The samples measured are the smallest single crystals studied so far by the μSR techniques.A complication in studying electron-doped HTSCs, is the electronic magnetic moments of the rare-earth ions. For example, their presence has prevented an accurate determination of the values of the magnetic penetration depth in the Meissner state [13, 14]. The $Pr_{2-x}Ce_xCuO_4$ compound is appealing for study, because the crystal-electric-field ground state of the Pr ion is non-magnetic.

In the next chapter an introduction to the μSR method is given. Chapter 3 provides a brief description of the crystal growth process, sample characteristics and the experimental setup. In Chapters 4 and 5, the experimental results are presented. A discussion of the results and conclusions are given in Chapter 6.

Chapter 2

μSR Spectroscopy

Muon spin rotation/relaxation (μSR) spectroscopy is an instrumental technique that utilizes the magnetic moment of a muon, primarily to probe the internal magnetic field distribution of a sample. The technique is extremely sensitive to both static and dynamic magnetism on an atomic scale. In this chapter a brief description of μSR and how it can be applied to measurements of the vortex state in a type-II superconductor is given.

2.1 Introduction

Muons (μ^+, μ^-) can be produced from the parity-violating decay of pions (π^+, π^-), which are produced from the collision of intermediate energy range (500-1000 MeV) protons [15] with a low atomic number target consisting of carbon or beryllium nuclei. Positive pions stopping near the downstream surface of the production target spontaneously decay after a mean life time of ~ 26 ns via

$$\pi^+ \longrightarrow \mu^+ + \nu_\mu \,. \tag{2.1}$$

Muons created in this way are called "surface muons". Since the neutrino is a left-handed particle (*i.e.* with its spin is directed antiparallel to its momentum direction) with spin $S = \frac{1}{2}$ and the pion at rest has a spin $S = 0$, conservation of linear and angular momentum requires that the decay muon has its spin pointing in a direction opposite to its linear momentum in the pion rest frame. By collecting the muons traveling in the same direction, a beam with relatively low kinetic energy (4.119 MeV) and a nearly 100% spin polarization is obtained. Thus, unlike conventional nuclear magnetic resonance (NMR), μSR benefits from a large initial spin polarization $\vec{P}_0$, independent of the sample or sample environment. Furthermore, as a $S = \frac{1}{2}$ probe, the muon has no electric quadrupole moment and hence is not directly sensitive to electric field gradients.

The muon has a mean lifetime of $\tau_\mu = 2.197\ \mu$s [16], after which it decays as follows

$$\mu^+ \longrightarrow e^+ + \nu_e + \overline{\nu}_\mu \,. \tag{2.2}$$

The probability of a decay positron with energy E emerging with a momentum at an angle θ with respect to the initial muon spin direction is [17]

$$dW(\varepsilon,\theta) \propto (3-2\varepsilon)\varepsilon^2[1+\frac{2\varepsilon-1}{3-2\varepsilon}\cos\theta]\,d\varepsilon\,d(\cos\theta)\,, \tag{2.3a}$$

$$\propto B(\varepsilon)[1+A(\varepsilon)\cos\theta]\,d\varepsilon\,d(\cos\theta)\,, \tag{2.3b}$$

where $\varepsilon = E/E_{max}$ is the reduced energy, $E_{max} = \frac{1}{2}m_\mu c^2 = 52.83$ MeV is the maximum possible relativistic positron energy and $A(\varepsilon)$ is the asymmetry factor. As shown in Fig. 2.1, the distribution of decay positrons is asymmetric. The asymmetry is a maximum (*i.e.* $A = 1$) when $\varepsilon = 1$, in which case no positrons are emitted antiparallel to the muon spin direction. The high energy positrons easily pass through components of the experimental apparatus (*e.g.* cryostat walls). They are detected by counters consisting of plastic scintillators, light guides and photomultipliers. The detection of the asymmetric distribution of

decay positrons provides a means of determining the time evolution of the spin polarization $\vec{P}(t)$ associated with an implanted ensemble of muons.

2.2 Time Differential μSR (TD-μSR)

In a time differential μSR experiment (Fig. 2.2), the muons pass through a plastic scintillator (muon counter **M**) placed in front of the sample (**S**), which starts an electronic clock (TDC $\equiv$ time-to-digital converter). Muons which miss the sample strike a scintillator detector placed behind the sample (veto counter **V**) and are rejected. A positron emitted from a muon stopping in the sample is detected by one of the surrounding counters (**U**, **D**, **L**, **R**, **B**, **F**). When this happens, the electronic clock is stopped and the event is recorded in a time histogram. The number of decay positrons that are detected per time bin Δt in the i^{th} counter is given by

$$N_i(t) = N_i^0 e^{-t/\tau_\mu}[1 + A_i^0 P_i(t)] + B_i\,, \tag{2.4}$$

where N_i^0 is a normalization constant, A_i^0 is the maximum asymmetry and B_i is the time-independent background associated with uncorrelated muon decay events. The single-counter "asymmetry" function is defined as $A_i(t) = A_i^0 P_i(t)$. One could also form the "two-counter asymmetry" by combining the time spectra from two detectors from the opposite side of the sample, *e.g.* **U**, **D** in Fig. 2.2 in the following way:

$$A_{U,D}(t) = \frac{N_U - N_D}{N_U + N_D}\,. \tag{2.5}$$

This eliminate operation the exponential contribution of the muon life time.

A good event in a TD-μSR experiment is defined as $\mathbf{M}\cdot\overline{\mathbf{V}}\cdot\mathbf{P}$, where $\mathbf{P} \equiv$ **U**, **D**, **L**, **R**, **B**, **F**. Depending on the directions of the external magnetic field and the muon-spin polarization, two or four of the **P** counters are employed. Often the initial muon-spin polarization

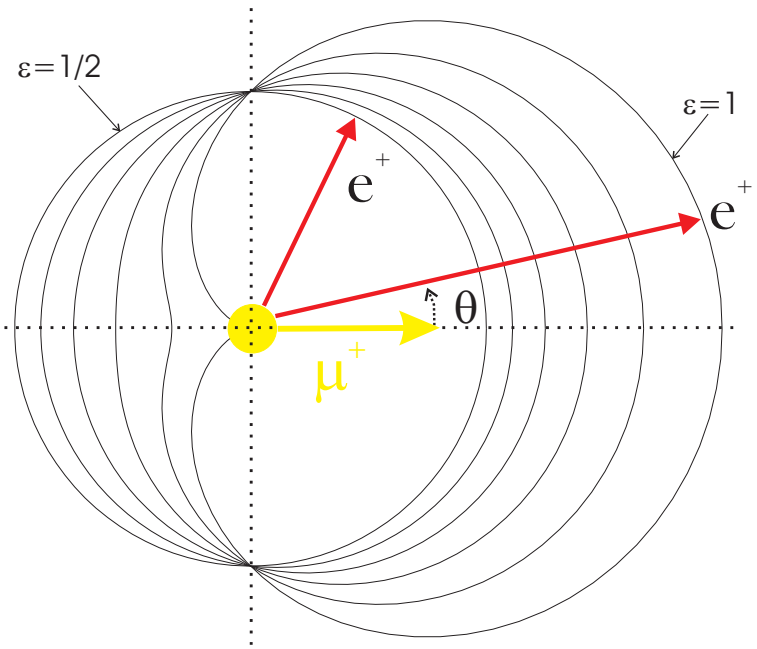

Fig. 2.1: Angular distribution of positrons from the μ^+ decay with respect to the initial muon spin direction. For $\varepsilon = 1$, the asymmetry of the distribution is a maximum. For $\varepsilon = 1/2$ (*i.e.* E = 26.415 MeV) the distribution is isotropic.

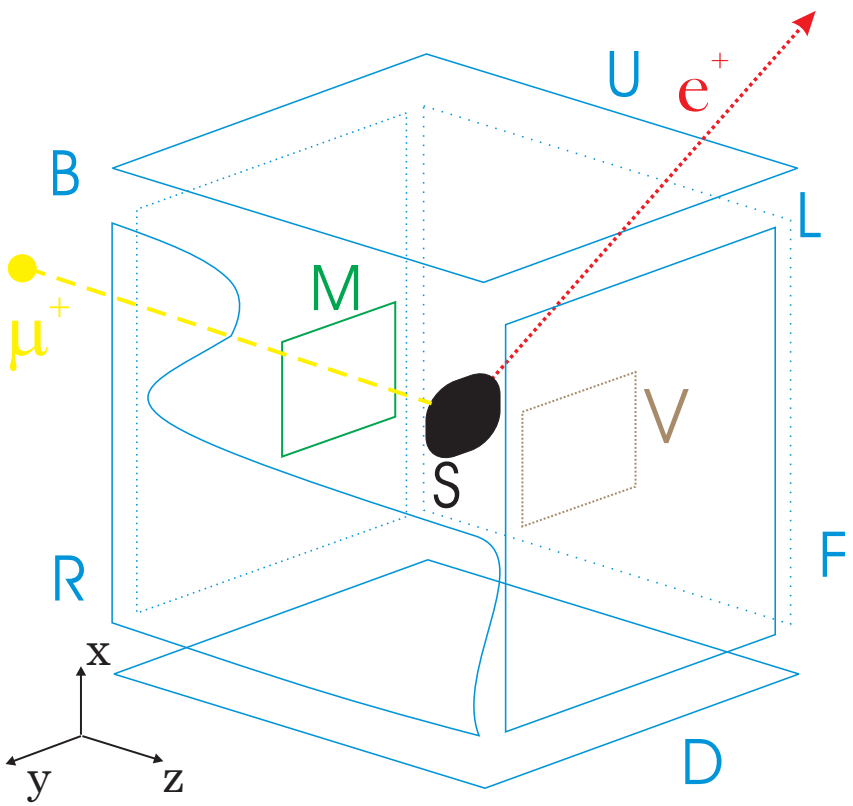

Fig. 2.2: Schematic diagram for a typical TD-μSR experiment. The μSR coordinate system convention is also shown at the lower left.

is rotated by 90° with respect to the beam momentum direction using a Wien filter (*i.e.* mutually perpendicular electric and magnetic fields) [18]. One reason for this is to avoid positron contamination from the beam in the **F** counter. The electronics is configurated to allow only one muon at a time in the sample, so that it is clear which muon a decay positron originates from. The "muon gate", which dictates how long one waits for a decay positron, is typically set to $\sim 10\,\mu$s. If the muon counter is triggered during this $10\,\mu$s window or the decay positron is not detected, no stop counts are recorded.

2.3 Transverse-Field μSR (TF-μSR)

In a transverse-field muon spin rotation experiment (Fig. 2.3), a magnetic field $\vec{H}$ is applied perpendicular to the initial muon-spin polarization direction. A muon stopping in the sample Larmor precesses about the local magnetic field $\vec{B}$ (which in general is different than the external field) at an angular frequency $\omega_\mu = \gamma_\mu B$, where $\gamma_\mu/2\pi = 135.5342\ \mathrm{MHz\,T^{-1}}$ is the muon gyromagnetic ratio.

In a superconductor the muons stop at well defined sites in the crystal lattice. However, in the vortex state of a type-II superconductor, the muons stop randomly on the length scale of the vortex lattice (which is typically two to three orders of magnitude larger than that of the crystal lattice). Consequently, μSR is an effective local probe of the spatial variation of internal magnetic fields due to the periodic arrangement of vortices. For the case where the external field is directed along $\hat{z}$, the x component of the muon-spin polarization function is

$$P_x(t) = \int_0^\infty n(B)\cos(\gamma_\mu B t + \phi)\,dB\,, \tag{2.6}$$

where $n(B)$ is the probability that a muon sees a local magnetic field between B and B+dB, and ϕ is the initial phase. There are several sources of the local magnetic field sensed

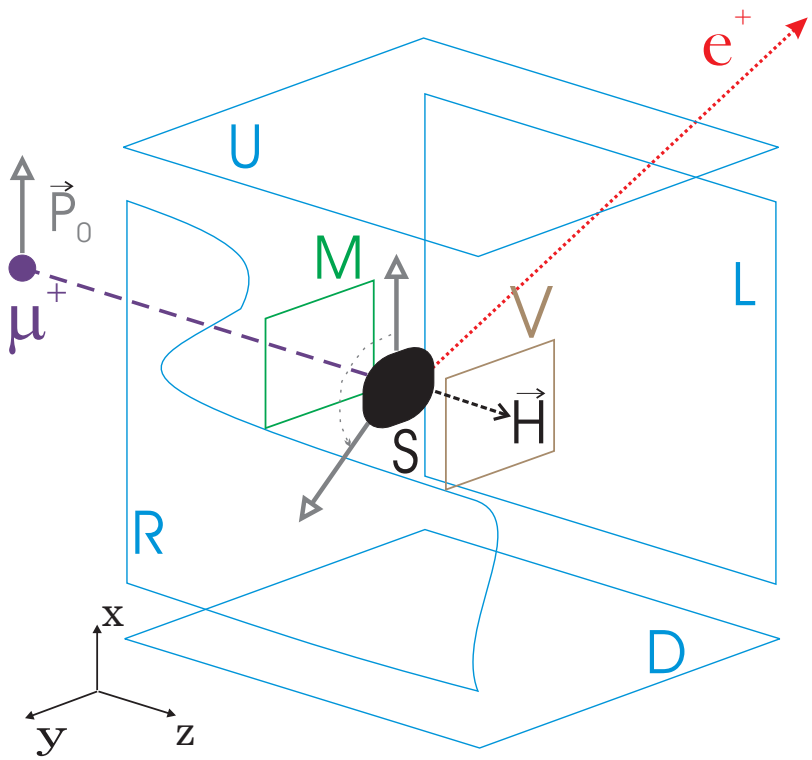

Fig. 2.3: Schematic diagram of a TF-μSR experiment. The initial muon spin polarization $\vec{P}_0$, indicated by the open arrow at μ^+, is rotated by 90° so that it is perpendicular to the direction of the external magnetic field $\vec{H}$. The open arrows at the sample **S** illustrate the Larmor precession of the muon spin.

by the muons. First there is the magnetic field inhomogeneity associated with the vortex lattice. For a type-II superconductor, the spatial profile of the magnetic field in the $\hat{a}$-$\hat{b}$ plane due to an applied field along the $\hat{c}$ axis ($\hat{z}$ direction) is reasonably described by the phenomenological model [19]

$$\vec{B}(\vec{r}) = B_0(1-b^4)\sum_{\vec{K}} \frac{e^{-i\vec{K}\cdot\vec{r}}uK_1(u)}{\lambda_{ab}^2K^2}\hat{z}, \tag{2.7}$$

where $\vec{K}$ is a reciprocal lattice vector, $b = B/B_{c_2}$ is the reduced field, $K_1(u)$ is a modified Bessel function and $u^2 = 2\xi_{ab}K^2(1+b^4)[1-2b(1-b)^2]$. Equation (2.7), which is derived from Ginzburg-Landau theory, assumes that $\lambda_{ab}^2K_{min}^2 \gg 1$, where K_{min}^2 is the magnitude of the smallest non-zero reciprocal-lattice vector in the summation. This condition is satisfied for an extreme type-II superconductor like the high-T_c cuprates, where $\lambda_{ab} \gg \xi_{ab}$. This self-consistent analytic function, agrees extremely well with the exact numerical solutions of the Ginzburg-Landau equations at low reduced fields b. Random vortex pinning and thermal fluctuations modify the field distribution associated with Eq. (2.7), which assumes a perfect periodic arrangement of vortices.

The muon is also sensitive to both nuclear and electronic dipole moments. The nuclear moments are randomly oriented at temperatures reachable in a μSR experiment (*i.e.* $T \geq 15$ mK), whereas electronic magnetic moments may order. In general, the magnetic moments that are static on the μSR time scale broaden the measured internal magnetic field distribution. To account for the effects of this additional source of field inhomomgeneity on the muon-spin polarization function, Eq. (2.6) can be multiplied by a depolarization function $G(t)$ such that

$$P_x(t) = G(t)\int_0^\infty n(B)\cos(\gamma_\mu Bt+\phi)\,dB\,. \tag{2.8}$$

The precise functional form of $G(t)$ depends on the nature of the additional sources of mag-

netic field at the muon site. For example, a Gaussian function $G(t) = \exp(-\sigma_{\rm dip}^2 t^2/2)$ with a depolarization rate $\sigma_{\rm dip}$, characterizes the damping of the muon-spin precession signal due to dense static dipole moments [20].

2.4 Fast Fourier Transform (FFT)

A common procedure often used to visualize the internal magnetic field distribution, is to perform a *fast Fourier transform* (FFT) of the muon-spin polarization function such that

$$n(B) = \int_0^\infty \tilde{P}(t) e^{-i(\gamma_\mu B t + \phi)}\, dt\,, \tag{2.9}$$

where $\tilde{P}(t) = P_x(t) + iP_y(t)$ is in general complex. However there are two limitations to the measured time spectrum that affect the FFT. First, due to the finite lifetime of the muon, there are fewer counts at the later times. Second, the length of the time spectrum is finite. These features introduce noise and "ringing" in the FFT spectrum. To smooth out these unwanted features, one can introduce an apodization function $\exp(-\sigma_A^2 t^2/2)$ such that

$$n(B) = \int_0^\infty \tilde{P}(t) e^{-i(\gamma_\mu B t + \phi)} e^{-\sigma_A^2 t^2/2}\, dt\,. \tag{2.10}$$

This procedure results in a time spectrum that smoothly goes to zero at later times. However, the drawback is that this introduces an additional source of broadening which also smooths out the the sharp features of interest. Nevertheless, FFTs remain useful as an approximate visual illustration of the internal magnetic field distribution and for comparing the measured μSR signal with the "best-fit" theory function from the time domain.

2.5 Zero-Field μSR (ZF-μSR)

One of the advantages of μSR spectroscopy over other magnetic resonance techniques (*i.e.* NMR, ESR) is that measurements can be performed in zero external magnetic field. In a zero-field muon-spin *relaxation* (ZF-μSR) experiment (Fig. 2.4), muons are used to probe the local magnetic field at their stopping site due to nearby nuclear and/or electronic magnetic moments. This is achieved by measuring the time evolution of the muon-spin polarization along its original direction (*i.e.* the relaxation function).

If the local magnetic fields are static, the muon will Larmor precess about the component of local field that is perpendicular to the muon spin. For the case of a sample with magnetic order, this gives rise to a muon-spin precession signal with a discrete frequency oscillation for each magnetically inequivalent muon site in the crystallographic lattice. The observed ZF relaxation function is

$$G(t) = \cos^2(\theta) + \sin^2(\theta)\cos(\gamma_\mu B t + \phi)\,, \tag{2.11}$$

where θ is the angle between the muon spin and the average static internal field $\vec{B}$.

The magnetic field distribution sensed by the muons in a system consisting of dense randomly oriented static magnetic moments is a Gaussian function. The corresponding relaxation function is given by the famous (Gaussian) Kubo-Toyabe (KT) function [21]

$$G^G_{\mathrm{KT}}(t) = \frac{1}{3} + \frac{2}{3}(1-\Delta^2 t^2)\exp\left(-\frac{\Delta^2 t^2}{2}\right), \tag{2.12}$$

where Δ is the relaxation rate and Δ^2/γ_μ^2 is the width of the magnetic field distribution at the muon site. Note that for early times ($t \ll \Delta^{-1}$) or for slow relaxation, Eq. (2.12) can be

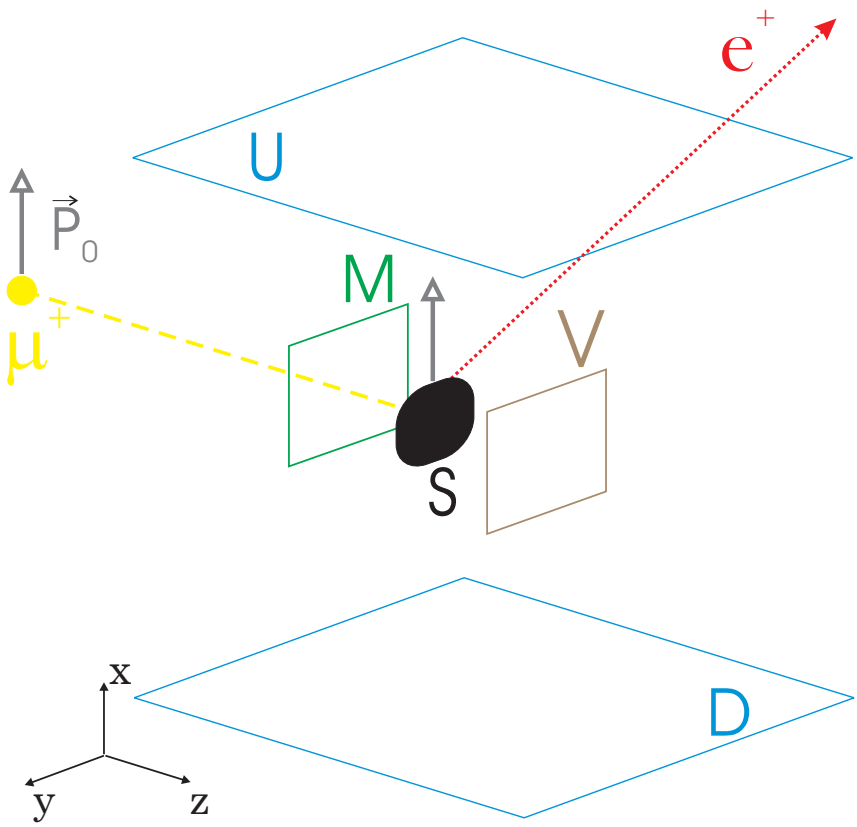

Fig. 2.4: Schematic diagram of a ZF-μSR experiment.

Taylor expanded as

$$\begin{aligned} G_{\mathrm{KT}}^{G}(t) &= \frac{1}{3}+\frac{2}{3}(1-\Delta^2t^2)(1-\frac{\Delta^2t^2}{2}+\frac{\Delta^4t^4}{8}-...)\,, \\ &\approx 1-\Delta^2t^2+\frac{5\Delta^4t^4}{12}-\ldots\,, \\ &\approx \exp(-\Delta^2t^2)\,. \end{aligned} \tag{2.13}$$

The Gaussian KT function is routinely used to describe nuclear magnetic moments, which are static on the μSR time scale.

A Lorentzian magnetic field distribution is sensed by the muons in a system consisting of dilute randomly oriented static magnetic moments (*i.e.* moments that are distributed randomly on less than 1% of the lattice sites). The corresponding relaxation function is a Lorentzian KT function [22]

$$G_{\mathrm{KT}}^{L}(t)=\frac{1}{3}+\frac{2}{3}(1-at)\exp(-at)\,, \tag{2.14}$$

where a is the relaxation rate. For early times ($t \ll a^{-1}$) or for slow relaxation, Eq. (2.14) can be Taylor expanded as

$$\begin{aligned} G_{\mathrm{KT}}^{L}(t) &= \frac{1}{3}+\frac{2}{3}(1-at)(1-at+\frac{a^2t^2}{2}-...)\,, \\ &\approx 1-\frac{4at}{3}+a^2t^2-\ldots\,, \\ &\approx \exp(-4at/3)\,, \\ &\equiv \exp(-\lambda t)\,, \end{aligned} \tag{2.15}$$

where $\lambda = 4a/3$ is the relaxation rate. The above KT functions describe dense/dilute randomly oriented static magnetic moments. For the situation where the local magnetism is intermediate between the dilute and dense limits, or dilute electronic magnetic moments (or magnetic clusters) are embedded in a system of concentrated nuclear dipoles, some combination of Eq. (2.13) and Eq. (2.15) is required.

If the magnetic moments in the sample are slowly fluctuating *i.e.* $\nu \ll \Delta$ where ν is the fluctuation rate, the "$1/3$ tail" in the KT functions relax to zero. If the magnetic moments are fluctuating at a high rate such that $\nu > \Delta$, the relaxation function then becomes an exponential function $\exp(-2\Delta t/\nu)$. For intermediate values of ν, the relaxation function has no analytical form.

Chapter 3

Experimental Details

In this chapter the growth process for the $Pr_{2-x}Ce_xCuO_4$ single crystals, the sample characteristics and the experimental setup used to perform the μSR measurements are briefly described.

3.1 Crystal Growth Process

The two single crystals studied were grown by Richard Greene's group at the University of Maryland, using a direct solidification technique [23]. A mixture of the compound $Pr_{2-x}Ce_xCuO_4$ and excess CuO powder was put in a Al_2O_3 crucible with a strong vertical temperature gradient. A CuO-based flux was added to lower the melting temperature. The mixture was then heated to about 1200-1300 K (T_{max}), and allowed to cool slowly (characterized by the *temperature ramp rate*) until the temperature dropped below the solidification temperature ($T \sim 1050$ K).

There are two main complications in the growth process of $Pr_{2-x}Ce_xCuO_4$ single crystals. The first problem is that for different Ce concentrations, optimal growth parameters

like (T_{max}) and the temperature ramp rate are different. The Ce concentration in the crystal is found to have no direct correlation with the Ce concentration of the mixture, but is closely related to T_{max} [24]. The optimal T_{max} must be carefully chosen to avoid a substantial Ce concentration gradient along the $\hat{c}$-axis direction of the crystal. The second problem is that the as-grown crystals are not superconducting. It is generally believed that a small amount of interstitial (apical) oxygen must be removed in order to achieve superconductivity. This was done by annealing the single crystal in an argon environment at a temperature 900-1000 K. However, due to the limited oxygen mobility, this reduction process often results in an oxygen gradient along the $\hat{c}$-axis direction, especially in crystals thicker than 50 μm. Increasing the annealing temperature or reduction time evaporates the Cu atoms, causing the surface of the crystal to decompose. A solution proposed by Brinkmann *et. al.* [24], and adopted by Greene's group, is to cover the entire crystal with polycrytalline $Pr_{2-x}Ce_xCuO_4$ pellets of the same composition during the annealing process. The pellets act as an effective Cu diffusion barrier. The introduction of a small amount of oxygen to the argon can speed up the process by increasing the annealing temperature without lowering T_c.

Contrary to widespread belief, there are some recent experiments suggesting that O(3) apical oxygen is not removed by the reduction process [25]. The role of oxygen in the superconductivity of electron-doped cuprates is a topic of current debate.

3.2 Sample Characteristics

Figure 3.1 shows the crystal structures of the electron-doped cuprate $Pr_{2-x}Ce_xCuO_4$ and the hole-doped cuprate $La_{2-x}Sr_xCuO_4$. The hole-doped compound has a T-phase structure where the copper atom is octahedrally coordinated with six oxygen atoms. On the other hand, $Pr_{2-x}Ce_xCuO_4$ has a T'-phase where there are no interstitial oxygen atoms.

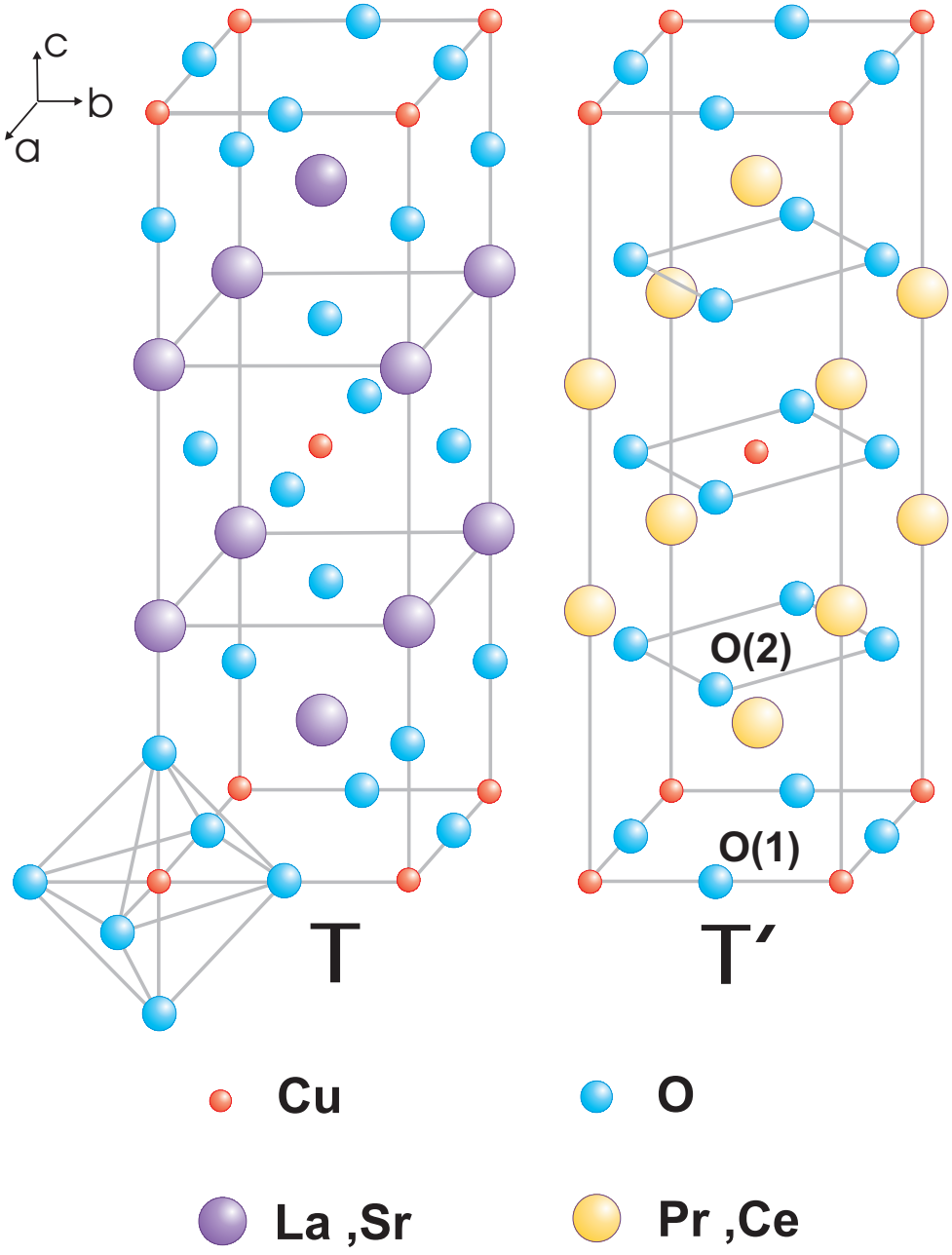

Fig. 3.1: Crystal structure of $La_{2-x}Sr_xCuO_4$ and $Pr_{2-x}Ce_xCuO_4$.

The results reported in this thesis are mainly from measurements on one of the single crystals, having a thickness of 0.07 mm, an $\hat{a}$-$\hat{b}$ plane surface area of ~ 6.5 mm^2 and a mass of 3.74 mg. It is the smallest single crystal measured by μSR using surface muons. Figure 3.2 shows the results of resistivity and bulk magnetic susceptibility measurements performed on this crystal. The resistivity measurements performed in zero external magnetic field, indicate that $T_c \approx 25 \pm 1$ K. This suggests that the crystal is near optimally doped with $x \approx 0.15$. However, the bulk magnetic susceptibility, measured using a Superconducting Quantum Interference Device (SQUID), reaches a constant value only below ~ 16 K. Given that resistivity measurements are sensitive to the "path of least resistance", the magnetic susceptibility is a better indication of the average value of T_c in the bulk of the sample.

3.3 Experimental Setup

The μSR experiments were carried out using both the M15 and M20B positive surface muon beam lines at TRIUMF. The measurements were taken using the LAMPF spectrometer, which consists of three orthogonal pairs of Helmholtz coils plus an array of counters to detect the decay positrons. These coils can be used to either apply a transverse magnetic field to the sample or to cancel out the external magnetic fields in a ZF-μSR experiment. To perform μSR experiments on such small crystals, the momentum of the incoming muons was reduced by about 4% so that sufficient muons stopped in the sample, rather than passing through. However, this also increases the contribution to the background signal from muons that are stopped upstream in the cryostat windows *etc*. To counteract this problem, the sample was sandwiched between a thin muon counter and the veto counter all contained inside a ^4He gas-flow cryostat, as shown in Fig. 3.3. A silver mask with a hole

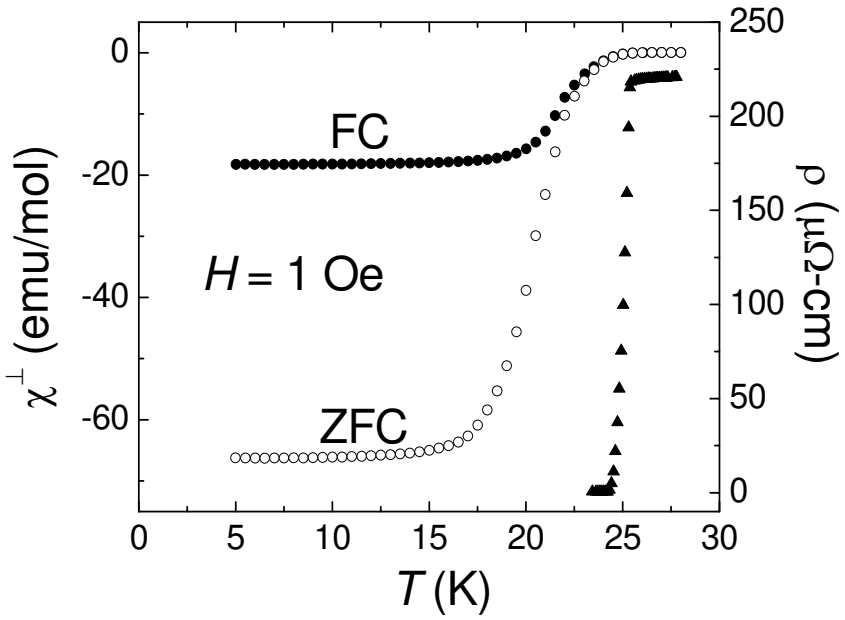

Fig. 3.2: Bulk magnetic susceptibility measurements taken under field-cooled (FC) and zero-field cooled (ZFC) conditions with $H = 1$ Oe and resistivity measurements (solid triangles) in zero external magnetic field. The applied field is directed along the crystallographic $\hat{c}$-axis.

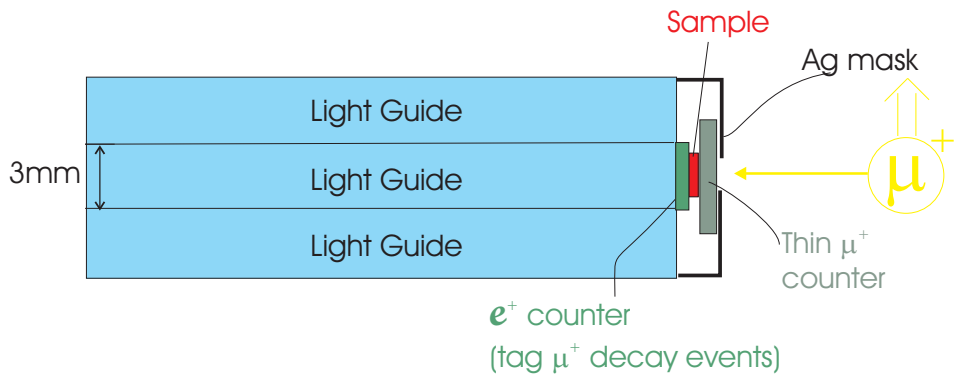

Fig. 3.3: Schematic of the experimental setup. All the components are contained within a ^{4}He gas-flow cryostat.

slightly smaller than the area of the sample was placed in front of the muon counter. Muons stopping in the mask do not pass through the muon counter and hence are logically excluded. While these muons still decay into positrons that are not logically excluded, we found that their contribution to the "uncorrelated" background signal was less than 10% of the good muon-decay count rate. Furthermore, with this experimental arrangement the μSR spectra contained no observable "correlated" background signal. To determine the value of the magnetic penetration depth, TF-μSR spectra with $\sim$ 20 million muon decay events were recorded.

Chapter 4

Zero-Field Measurements

In this chapter, zero-field (ZF) μSR measurements on the $Pr_{2-x}Ce_xCuO_4$ single crystals are presented. For all measurements described here, the initial muon-spin polarization $\vec{P}(0)$ was directed parallel to the CuO_2 layers.

Figure 4.1 shows the time evolution of the two-counter asymmetry at T = 165 K, 80 K, 40 K and 2.3 K in the absence of an external magnetic field. The lack of any discrete frequency oscillations in the ZF-μSR signals indicates that there is no onset of magnetic order at temperatures $T \geq 2.3$ K.

To gain further insight into the nature of the magnetism which relaxes the ZF-μSR signal, a constant magnetic field was applied along the direction of the initial muon-spin polarization. This arrangement is known as a *longitudinal-field* (LF) μSR experiment. Muons implanted in the sample precesses about the local magnetic field, which is a vector sum of the applied field and the local internal magnetic fields due to nuclear and electronic magnetic moments. If the internal magnetic field is static and a large external magnetic field H is applied along the direction of the initial muon-spin polarization $\vec{P}(0)$, the component of the resultant magnetic field perpendicular to $\vec{P}(0)$ will be small. Consequently the applied

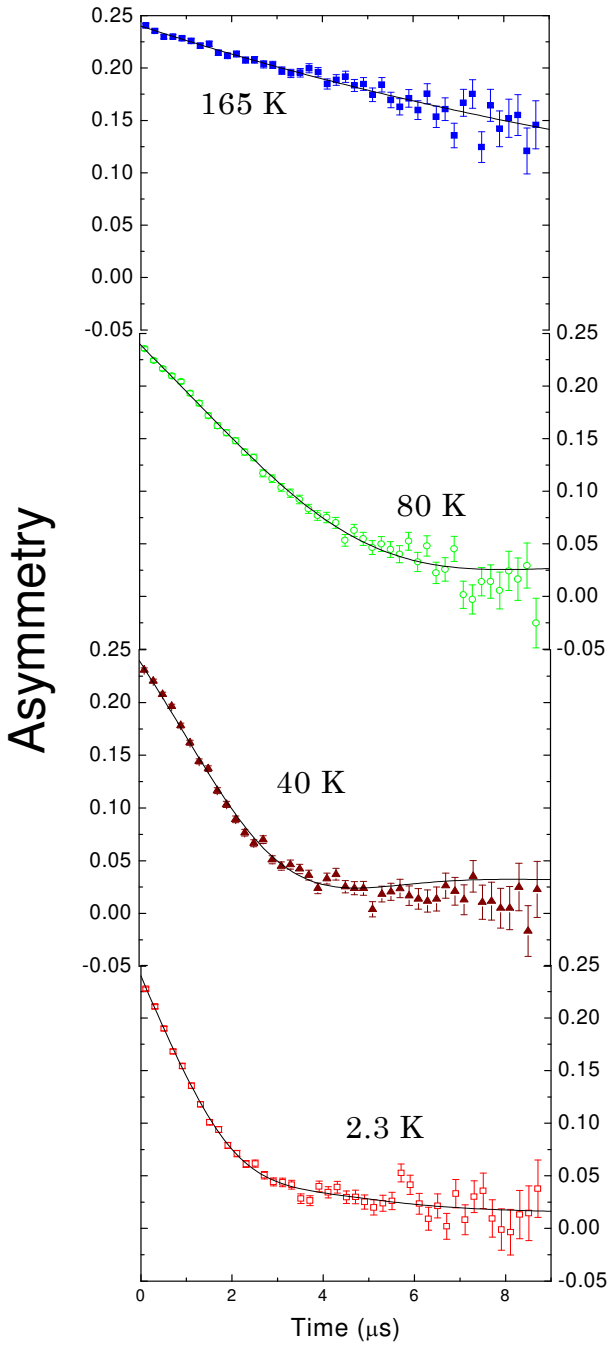

Fig. 4.1: Time evolution of the asymmetry in zero external magnetic field at T = 165 K, 80 K, 40 K and 2.3 K. The solid curves are fits to Eq. (4.1)

.

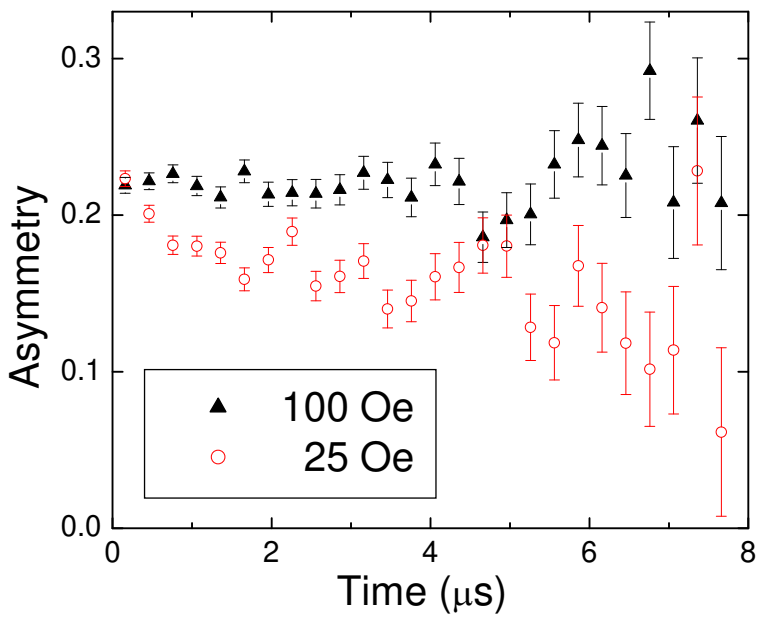

Fig. 4.2: Time evolution of the asymmetry in longitudinal external magnetic fields of 100 Oe and 25 Oe, at T = 25 K. The direction of both the external magnetic field and the initial muon-spin polarization are parallel to the CuO_2 layers. The scatter in the data is due to low statistics ($\sim$ 1 million muon-decay events).

magnetic field decouples the muon spin from the local static magnetic fields [15]. Figure 4.2 shows the time evolution of the asymmetry for applied longitudinal fields of H = 100 Oe and 25 Oe at T = 25 K. A longitudinal field of 100 Oe is large enough to completely decouple the muon spin from the local magnetic field, evident by the non-relaxing asymmetry over the 8 μs time range. This indicates that the magnetism in the sample at 25 K is fluctuating at a rate of less than 1 MHz. As the Pr^{3+} ions have a non-magnetic singlet ground state and the local magnetic field due to the nuclear magnetic moments is small (*i.e.* 10^2-10^3 times smaller than that of the electronic magnetic moments), the dominant source of local magnetism must be from Cu spins.

The solid curves in Fig. 4.1 are fits to the following relaxation function [26].

$$G(t) = a_1[\frac{1}{3} + \frac{2}{3}(1-\Delta^2 t^2)\exp((-\Delta^2 t^2)/2)] + a_2\exp(-\lambda t), \tag{4.1}$$

where $a_1 + a_2 = 1$, and Δ and λ are the Gaussian and exponential relaxation rates, respectively. Assuming that there is only one muon stopping site, the first term corresponds to the relaxation of the muon-spin polarization due to muons seeing only nuclear dipole moments. The second term is the relaxation due to muons which see dilute magnetic moments or magnetic clusters. Figure 4.3 shows the temperature dependence of a_1 and a_2. The exponential relaxation (*i.e.* $a_1 = 0$) at high temperature is likely due to "fast" fluctuating Cu spins, although this has not been verified by LF-μSR measurements. At $T \sim 60$ K, $a_1 \approx a_2$. This indicates that the dilute magnetic moments are found in 50% of the sample volume. As the temperature is lowered, a_1 decreases and a_2 increases, indicating that the dilute magnetic regions grow in size. Figure 4.4 shows the temperature dependence of the relaxation rates Δ and λ. As the temperature is lowered, the relaxation rates increase monotonically. This is consistent with a broadening of the magnetic field distribution due to gradual slowing down of the Cu spins.

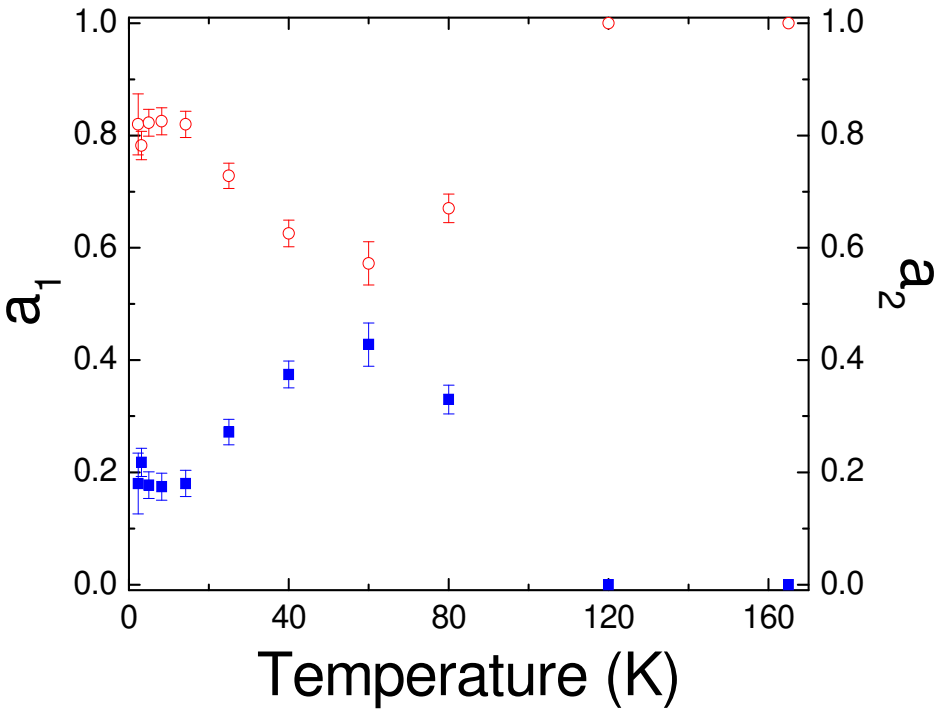

Fig. 4.3: Temperature dependence of the amplitudes a_1 (solid squares) and a_2 (open circles) from Eq. (4.1). Note that $a_1 + a_2 = 1$.

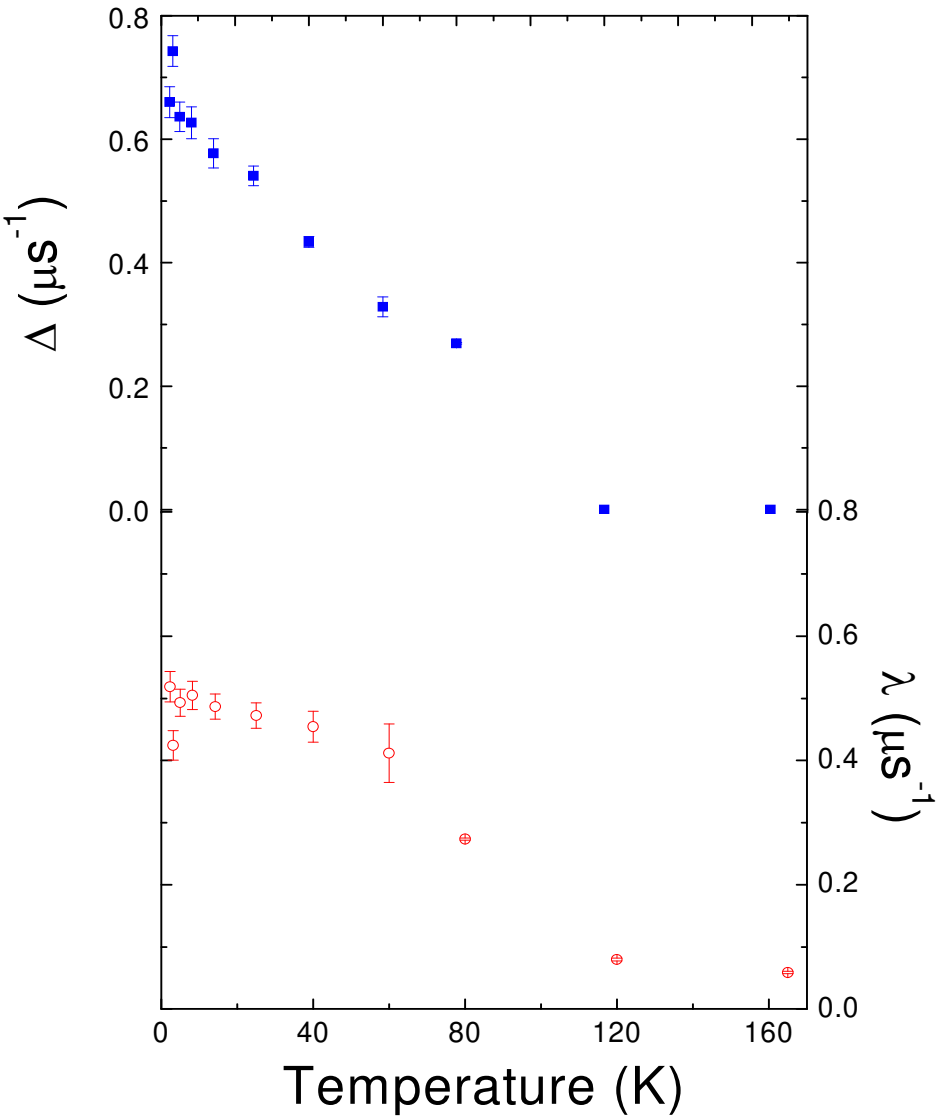

Fig. 4.4: Temperature dependence of the relaxation rates Δ (solid squares) and λ (open circles) from Eq. (4.1).

Chapter 5

Transverse-Field Measurements

In this chapter, transverse-field (TF) μSR measurements on the $Pr_{2-x}Ce_xCuO_4$ single crystals are presented. For all the measurements described here, the initial muon-spin polarization $\vec{P}(0)$ was directed parallel to the CuO_2 layers while the applied magnetic field H was directed perpendicular to the CuO_2 layers.

Figure 5.1 shows the time evolution of the muon-spin polarization taken under field-cooled (FC) and zero-field cooled (ZFC) conditions at $T = 2.4$ K. In the FC procedure, the sample is cooled to temperatures below T_c in an applied magnetic field. Generally speaking, for intermediate applied fields $H_{c_1} < H < H_{c_2}$, this results in a well-ordered vortex lattice in the superconducting state. Consequently, the time spectra show an oscillating signal with an amplitude damped out over time due to the inhomogeneous internal magnetic field distribution of the vortex lattice. In the ZFC procedure, the sample is cooled below T_c in zero external magnetic field and then an external field is applied. In this case, pinning at the sample edges usually prevents the magnetic flux from entering the bulk of the sample at low external magnetic fields ($H \leq 300$ Oe). Consequently the ZFC asymmetry spectra resemble those in the ZF measurements. At higher field ($H = 500$ Oe) under ZFC conditions, the

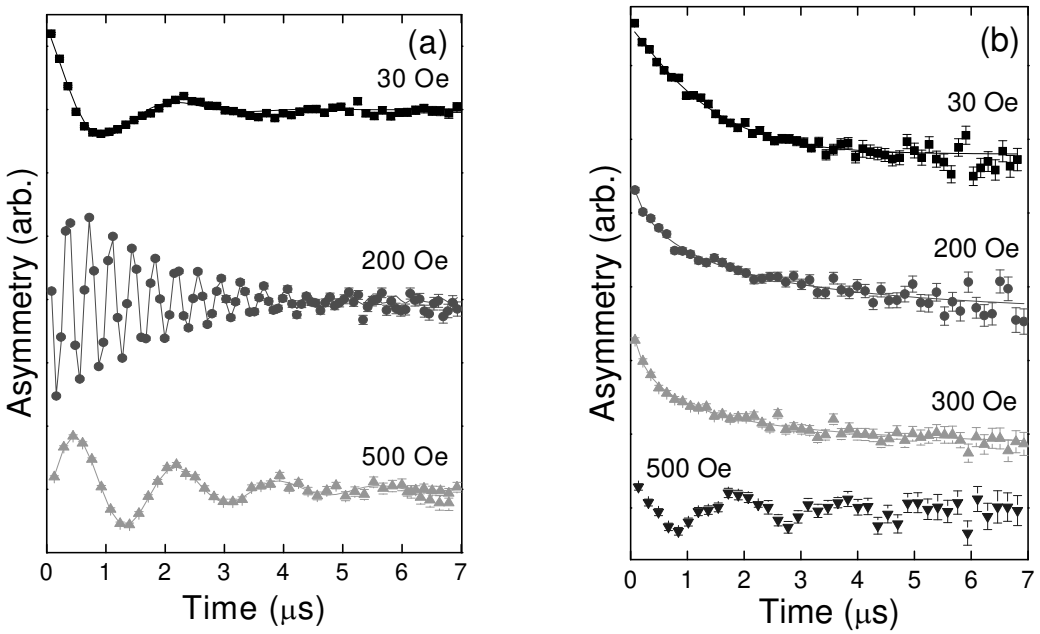

Figure 5.1: Time evolution of the muon-spin polarization in $Pr_{2-x}Ce_xCuO_4$ taken under (a) FC and (b) ZFC conditions at T = 2.4 K. Note that the time spectrum at H = 500 Oe is presented in the rotating reference frame.

magnetic flux fully penetrates the bulk of the sample, but in the absence of a strong repulsive interaction between the vortices, random defects in the sample exert a pinning force on the vortices, resulting in a highly disordered arrangement.

Figure 5.2 shows the time evolution of the muon-spin polarization taken under FC and ZFC conditions at H = 91 Oe at a number of temperatures. In the FC procedure [Fig. 5.2(a)], the muon-spin depolarization rate decreases with increasing temperature due to the growth of the in-plane magnetic penetration depth λ_{ab}, which is the length scale over which magnetic field decays outside of the vortex core. On the other hand, under ZFC conditions [Fig. 5.2(b)], pinning at the sample surface prevents the magnetic flux from entering the bulk of the sample at low temperatures. At higher temperature (10 K), magnetic flux pene-

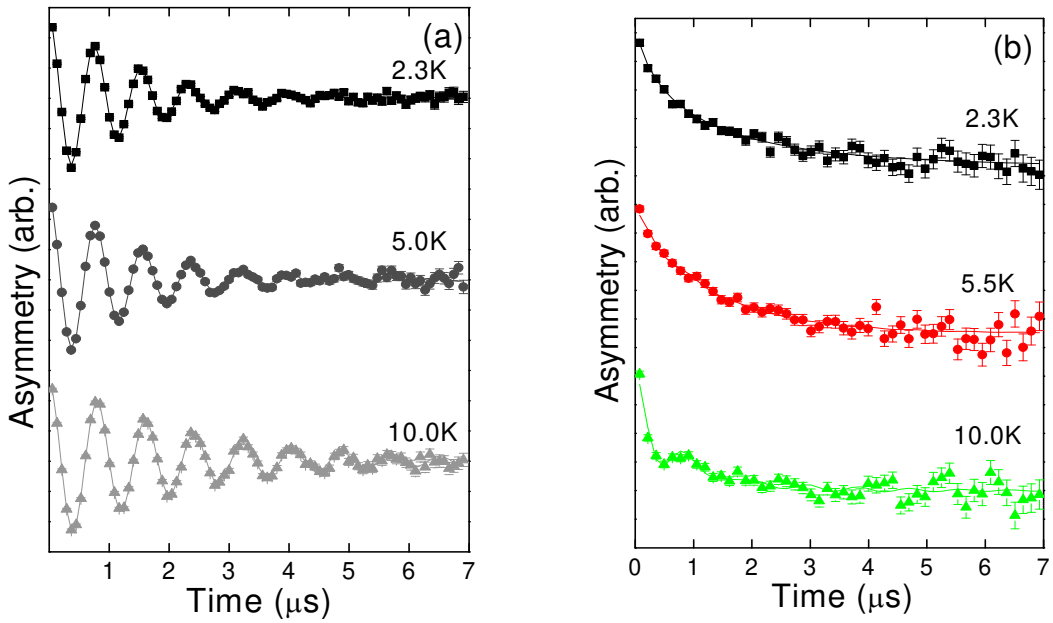

Figure 5.2: Time evolution of the muon-spin polarization in $Pr_{2-x}Ce_xCuO_4$ taken under (a) FC and (b) ZFC conditions at $H = 91$ Oe.

trates deeper into the sample due to thermal depinning and an increase of λ_{ab}.

Figure 5.3 shows fast Fourier transforms (FFTs) of the muon-spin precession signals at $H = 91$ Oe recorded under FC conditions. To eliminate systematic errors, these measurements were taken at different temperatures in a random sequence. The FFTs give an approximate picture of the internal magnetic field distribution $n(B)$. Although the sharp features of $n(B)$ are smeared due to the effects described in section 2.4, the FFTs still provide useful insight into the nature of $n(B)$. Above T_c, the field distribution is broadened by both the electronic and nuclear magnetic moments. The μSR linewidth was observed to increase with increasing H. This behaviour suggests that there is an inhomogeneous distribution of local magnetic susceptibilities in the sample, which results in a distribution of muon fre-

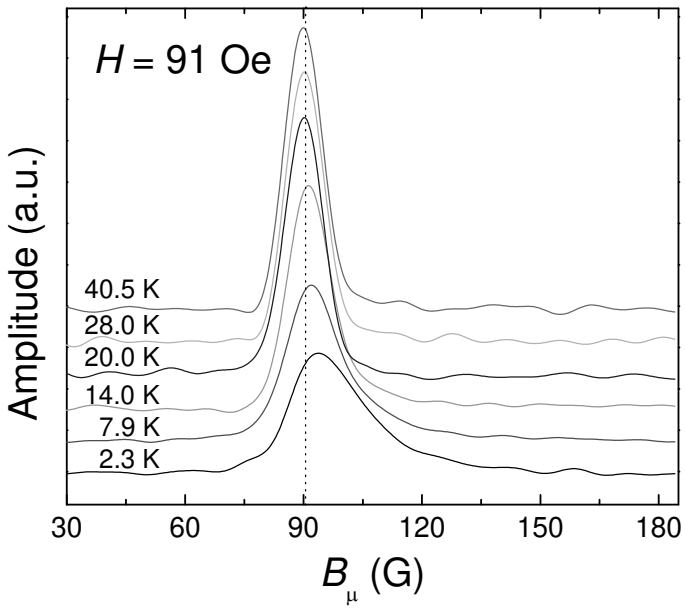

Fig. 5.3: FFTs of the muon-spin precession signal in $Pr_{2-x}Ce_xCuO_4$ plotted as a function of the local magnetic field B_μ sensed by the muons. The value of the external magnetic field (H = 91 Oe) is represented by the vertical dashed line.

quency shifts. It is likely that the inhomogeneity arises from spatial variations of charge doping. Below T_c, the field distribution is further broadened and becomes asymmetric, due to the inhomogeneous field produced by a vortex lattice. To minimize the effects of the inhomogeneous local magnetic susceptibility, the magnetic penetration depth measurements were performed at low external magnetic fields.

In Nd_2CuO_4, which is the parent compound of the related electron-doped cuprate $Nd_{2-x}Ce_xCuO_4$, the muon stopping site was found to be near an O(2) oxygen midway between two CuO_2 planes [2] (Fig. 3.1). In particular, the implanted muon hydrogen bonds to the oxygen ion with a bonding radius of ~ 1 Å. This single muon stopping site assignment is consistent with Fig. 5.3, which shows only one well-resolved signal with an average frequency shift relative to the Larmor precession frequency of the positive muon in vacuum.

Figure 5.4 shows the temperature dependence of the difference between the average local magnetic field B_0 at the muon site and the external magnetic fields H = 91 Oe, 200 Oe, 500 Oe and 2000 Oe. The open circles represent measurements at H = 200 Oe on a second $Pr_{2-x}Ce_xCuO_4$ single crystal. Above T_c, B_0 - $\mu_0 H$ is a linear function of H (see inset of Fig. 5.4) which corresponds to a μ^+ Knight shift,

$$K_\mu^\perp = \frac{B_0 - \mu_0 H}{\mu_0 H}\,. \tag{5.1}$$

Note that "$\perp$" refers to H directed perpendicular to the CuO_2 plane. This is the measured μ^+ Knight shift. The intrinsic μ^+ Knight shift is obtained after correcting for the sample geometry such that,

$$K^\perp = K_\mu^\perp + (\frac{1}{3} - N)\chi^\perp\,, \tag{5.2}$$

where N is a geometrical demagnetization factor that reduces the effective local field sensed by the muons. In particular, the demagnetization field is given by

$$\vec{B}_{dem} = -\mu_0 N \vec{M}\,, \tag{5.3}$$

where $\vec{M} = \chi^\perp \vec{H}$. For a thin plate-like crystal $N \approx 1$. The $\frac{1}{3}$ factor in Eq. (5.2) is due to the Lorentz field [20], $\vec{B}_L = \mu_0 \vec{M}/3$.

Figure 5.5 shows a plot of the intrinsic μ^+ Knight shift $K^\perp$ against the measured bulk magnetic susceptibility $\chi^\perp$. The negative value of $K^\perp$ in the normal state results from the dipolar fields of electronic Pr magnetic moments, which are induced by the external magnetic field. Below T_c, the average internal magnetic field increases such that for low H, B_0 is actually greater than the value of the applied field. This is unusual because a fundamental property of a superconductor is it that it expels magnetic field. In contrast to the normal state, B_0 - $\mu_0 H$ is not a linear function of H and is reduced with increasing H.

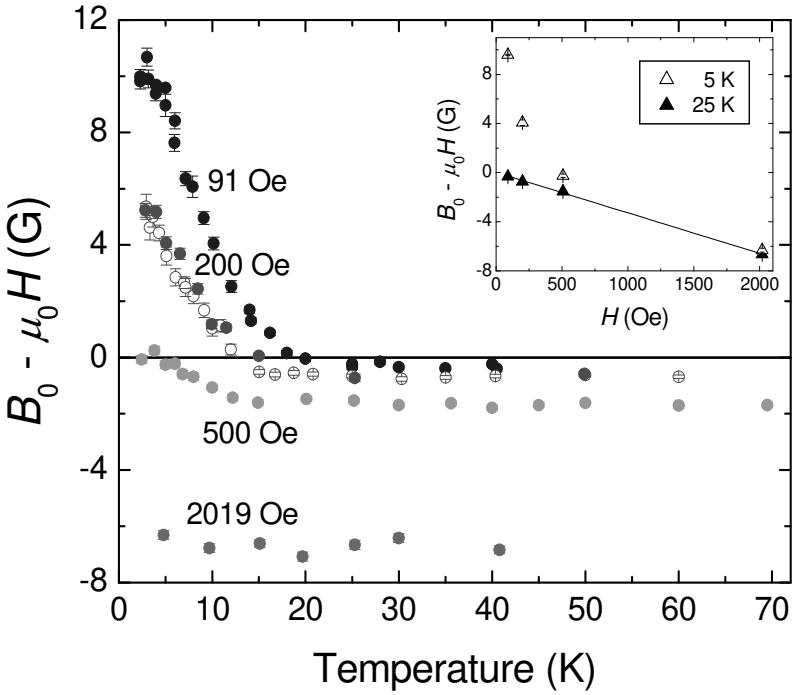

Fig. 5.4: Temperature dependence of the difference between the average local magnetic field B_0 at the muon stopping site and the external magnetic field H = 91, 200, 500 and 2019 Oe. The open circles represent measurements on a second $Pr_{2-x}Ce_xCuO_4$ single crystal at H = 200 Oe. Inset: Magnetic field dependence of $B_0 - \mu_0 H$ at T = 5 and 25 K.

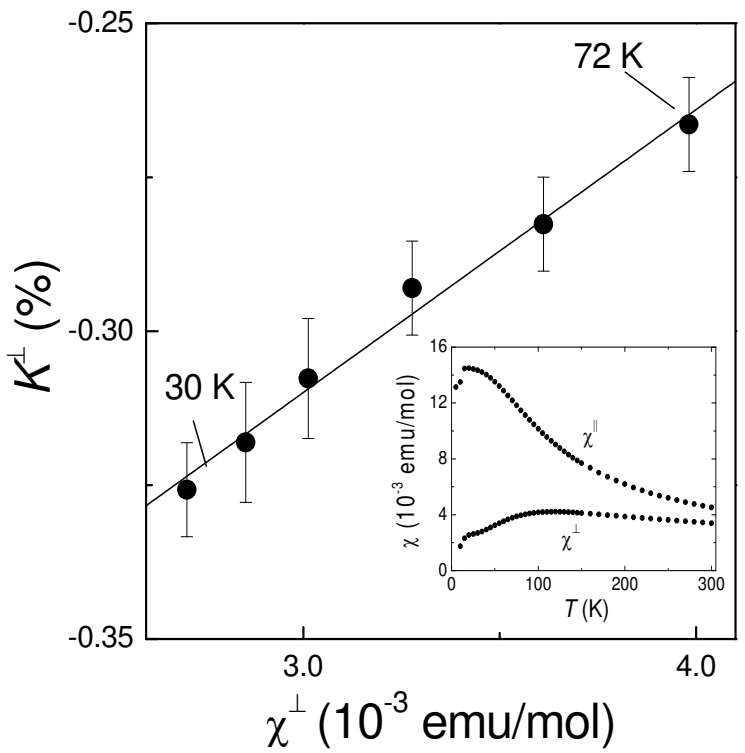

Fig. 5.5: The intrinsic μ^+ Knight shift$K^{\perp}$ vs. the bulk susceptibility $\chi^{\perp}$ at H = 3 kOe. Inset: Temperature dependence of the bulk magnetic susceptibility measured in an external magnetic field H = 10 kOe applied perpendicular ($\chi^{\perp}$) and parallel ($\chi^{\parallel}$) to the $\hat{a}$-$\hat{b}$ plane.

As shown in Fig. 5.6, the increase of B_0 with decreasing temperature nearly coincides with the diamagnetic shift observed below T_c in bulk magnetic susceptibility measurements taken under FC conditions. Such behaviour could be associated with the so-called *paramagnetic Meissner effect* (PME) [27], which is a reported anomalous paramagnetic response in dc FC magnetization measurements. However, magnetization measurements taken under both FC and ZFC conditions show a diamagnetic response that is inconsistent with this interpretation. A second possible explanation is that the Pr electronic moments induce screening currents in the CuO_2 planes [28]. However, unlike the large rare-earth moments in the $RBa_2Cu_3O_7$ (R $\equiv$ Gd, Er) compound studied in Ref. [28], the Pr moments induced at low fields are too weak to induce a significant shift of the local magnetic field. In particular, at $H = 90$ Oe and $T = 25$ K (see Fig. 5.4 inset), B_0 - $\mu H \approx -0.3$ G, whereas B_0 - $\mu H \approx 10$ G at $T = 5$ K.

A third possible origin of the increased internal magnetic field below T_c is that the vortices stabilize magnetic order of the Cu spins. This has recently been observed in a neutron scattering study of underdoped $La_{2-x}Sr_xCuO_4$ ($x = 0.1$) single crystals [29]. Although the difference between the average local magnetic field in the superconducting state (B_0^S) and the normal state (B_0^N) of $Pr_{2-x}Ce_xCuO_4$ decreases as H increases, it does not necessarily imply that the additional magnetism below T_c weakens with increasing H. Figure 5.7 shows a plot of B_0^S - B_0^N as a function of B_0^N at temperatures $T = 5$ K and 10 K. The solid curves are fits to the relation

$$B_0(T) = \sqrt{(B_0^N)^2 + B_{||}^2}, \tag{5.4}$$

where $B_{||}$ is an additional component of field in a direction perpendicular to B_0^N. These fits give $B_{||} = 43$ G and 26 G at $T = 5$ K and 10 K, respectively. The quality of these fits indicate that the orientation of the additional field that appears at the muon site below T_c is directed

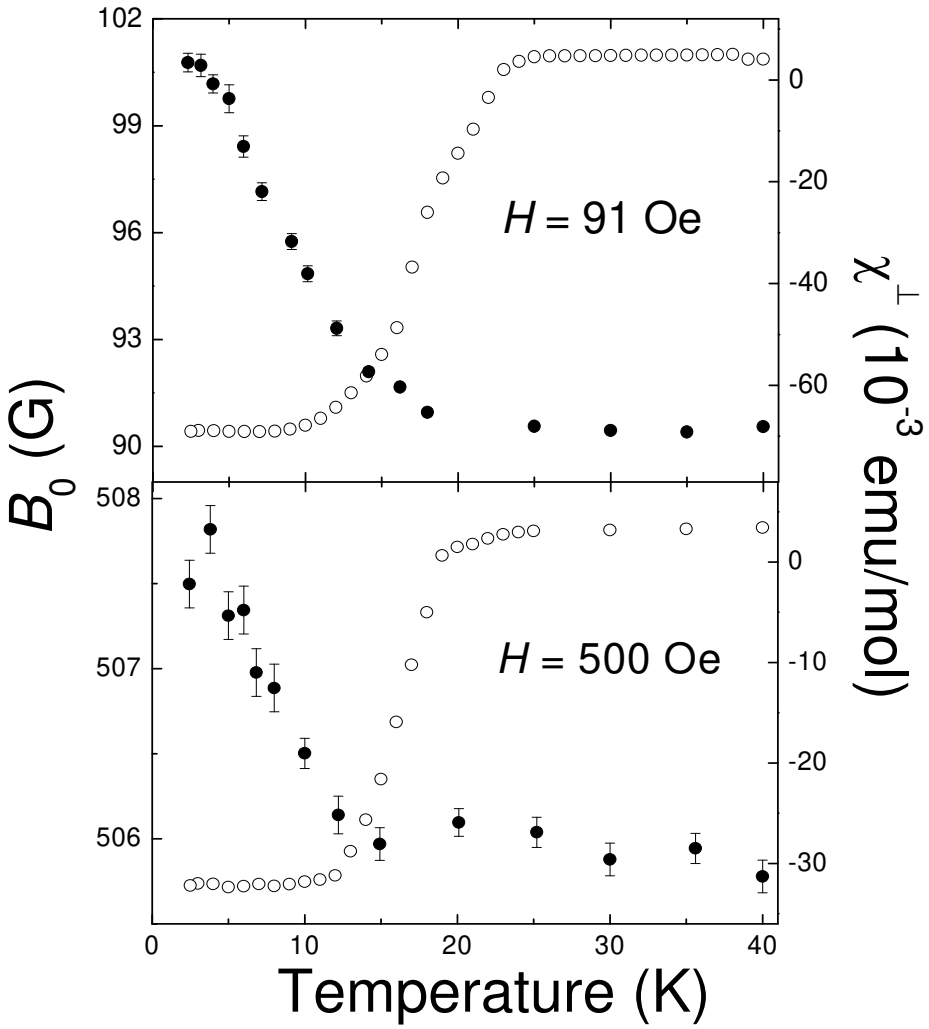

Fig. 5.6: Temperature dependence of the average local magnetic field at the μ^+ stopping site B_0 (solid circles) and the bulk magnetic susceptibility $\chi^{\perp}$ (open circles) measured under FC conditions at H = 91 and 500 Oe.

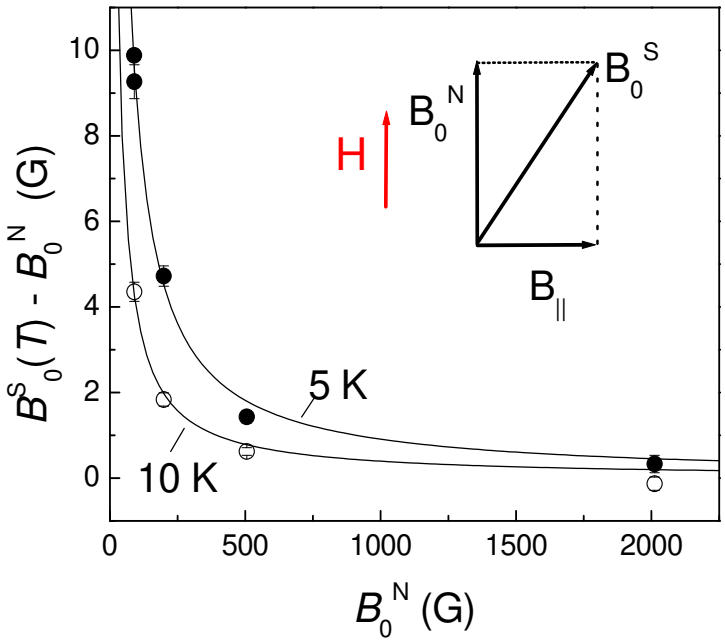

Fig. 5.7: Magnetic field dependence of B_0^S - B_0^N at T = 5 K (closed circles) and 10 K (open circles). The solid curves are fits of the data to Eq. (5.4) with $B_{||}$ as a free parameter.

primarily parallel to the CuO_2 planes.

Figure 5.8 shows two proposed Cu-spin structures for the parent compound Pr_2CuO_4 [30, 31]. In both structures, the Cu spins are antiferromagnetically ordered in the CuO_2 planes. However, in the collinear structure, Cu-spins in adjacent CuO_2 planes are aligned either parallel or antiparallel to each other, whereas in the non-collinear structure, Cu-spins in adjacent CuO_2 planes are aligned perpendicular to one another. Also shown in Fig. 5.8 is a plot of the calculated magnitude of the magnetic field at the muon stopping site due to the dipolar fields of the Cu moments as a function of the canting angle θ between the Cu spins and the CuO_2 plane. The calculation assumes the ordered Cu moment value of 0.40 μ_B determined by neutron scattering in Pr_2CuO_4 [30]. The same field-dependent neu-

tron scattering measurements suggest that the correct Cu-spin structure is the non-collinear one. Our calculation shows for both Cu-spin structures, the magnitude of the magnetic field at the muon stopping site due to the Cu moments is the same. It also shows that this magnetic field is directed parallel to the CuO_2 plane. This indicates that the onset of antiferromagnetic order is the source of the additional local magnetic field sensed by the muons below T_c.

To determine the in-plane magnetic penetration depth λ_{ab}, the individual time histograms from the four counters (**U**, **D**, **L**, **R**) were fit simultaneously to Eq. (2.4), assuming the spatial magnetic field profile given by Eq. (2.8). To model the effect of the internal magnetism due to electronic and nuclear moments on the muon-spin precession signals, several depolarization functions $G(t)$ were tested. For example, we first tried $G(t) = e^{-\sigma^2 t^2/2}$ and $G(t) = e^{-\Delta t}$ which assumes these static magnetic moments are dense and dilute respectively. In the final analysis a power exponential function, $G(t) = \exp[-(\Delta t)^{\beta}]$, with the value of β fixed to 1.2. This gave fits of similar quality over the whole temperature range below T_c. Figure 5.9 shows the FFTs of the muon-spin precession signal and the two different "best-fit" theory functions from the time domain at $T = 3.15$ K. The FFT of the fit function with $G(t) = e^{-(\Delta t)^{1.2}}$ clearly gives a more accurate representation of the measured internal magnetic field distribution than that with $G(t) = e^{-(\sigma t)^2/2}$.

At low external magnetic field, where the density of vortices is small, few muons stop in the vicinity of the vortex cores. Consequently, measurements at low H here are not sensitive to the high-field cutoff of the measured field distribution, which corresponds to the vortex core region. This prevents an accurate determination of ξ_{ab}. Figure 5.10 shows the temperature dependence of the in-plane magnetic penetration depth determined with the value of ξ_{ab} fixed in the fitting procedure. The plot shows results for two different values

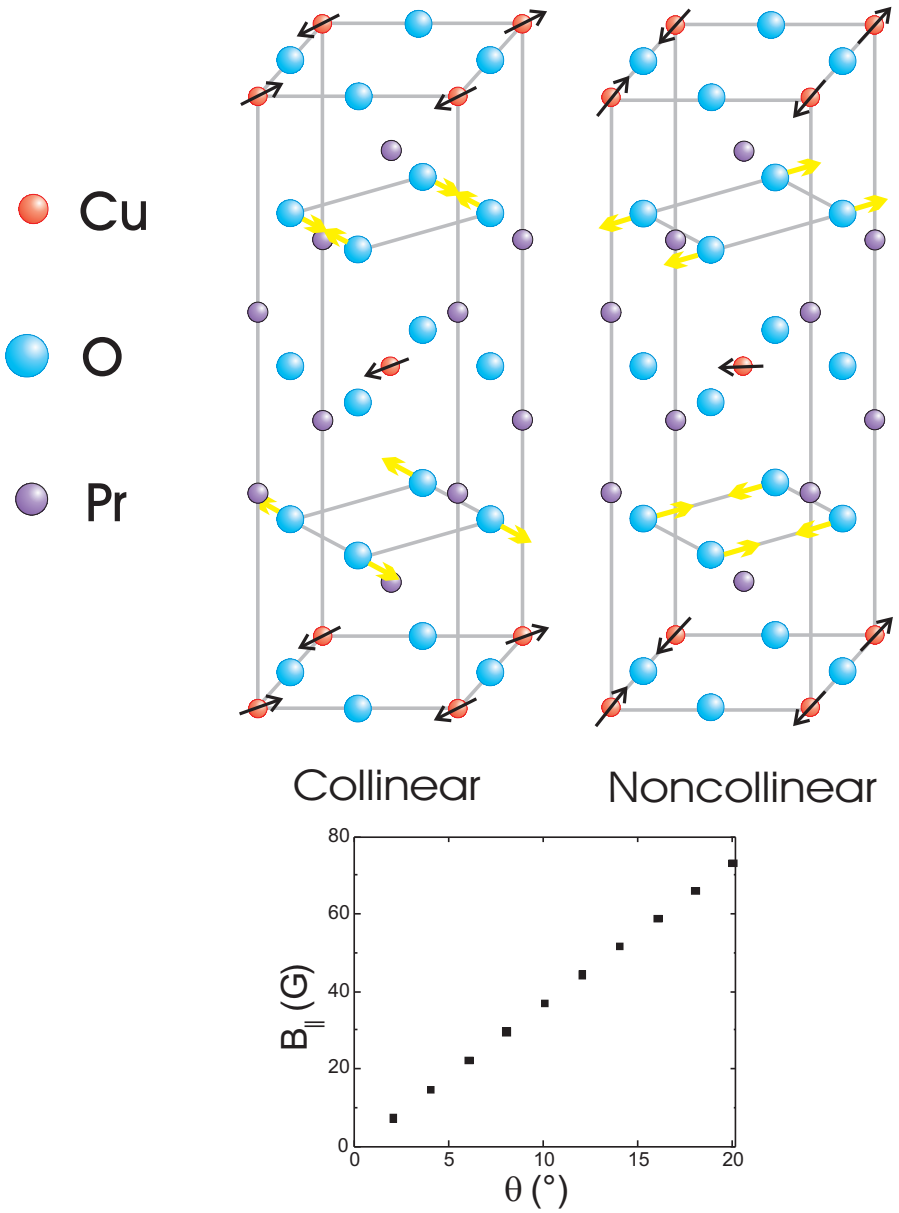

Fig. 5.8: Top: Two proposed ordered Cu-spin structures for Pr_2CuO_4. Bottom: Magnetic field strength at the muon stopping site due to Cu dipole moments plotted as a function of the canting angle θ between the Cu spins and the CuO_2 plane. The arrows at the oxygen atoms indicate the direction of the net local magnetic field due to the Cu moments. The results are the same for both models.

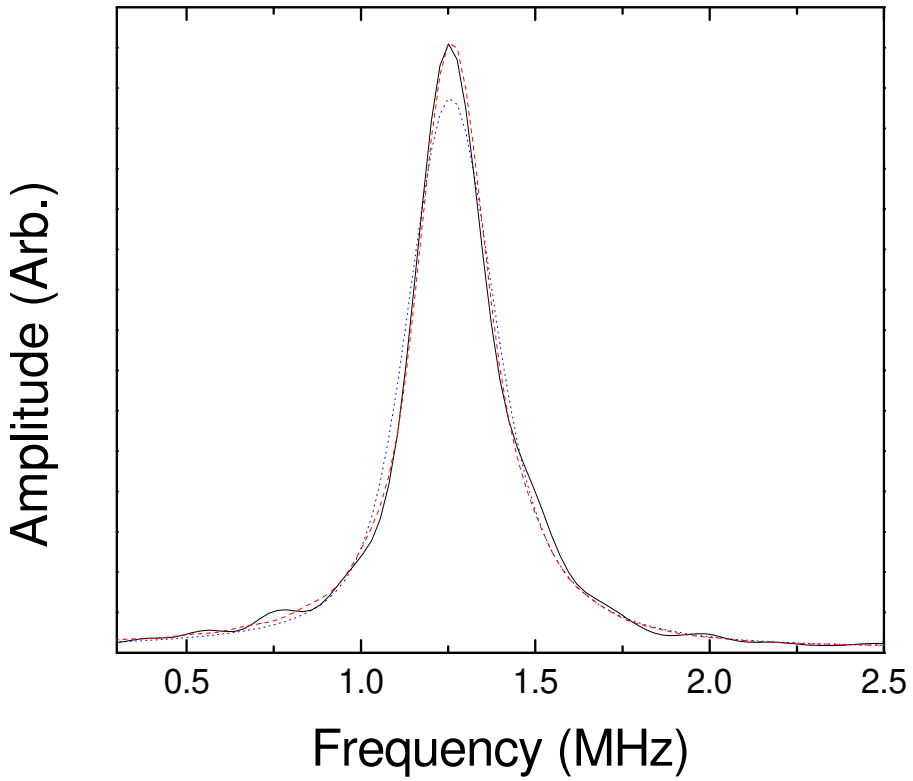

Fig. 5.9: FFTs of the muon-spin precession signal (solid line) and the theoretical muon-spin polarization functions with $G(t) = e^{-(\Delta t)^{\beta}}$ where $\beta = 1.2$, (dashed line) and $G(t) = e^{-(\sigma^2 t^2)/2}$ (dotted line).

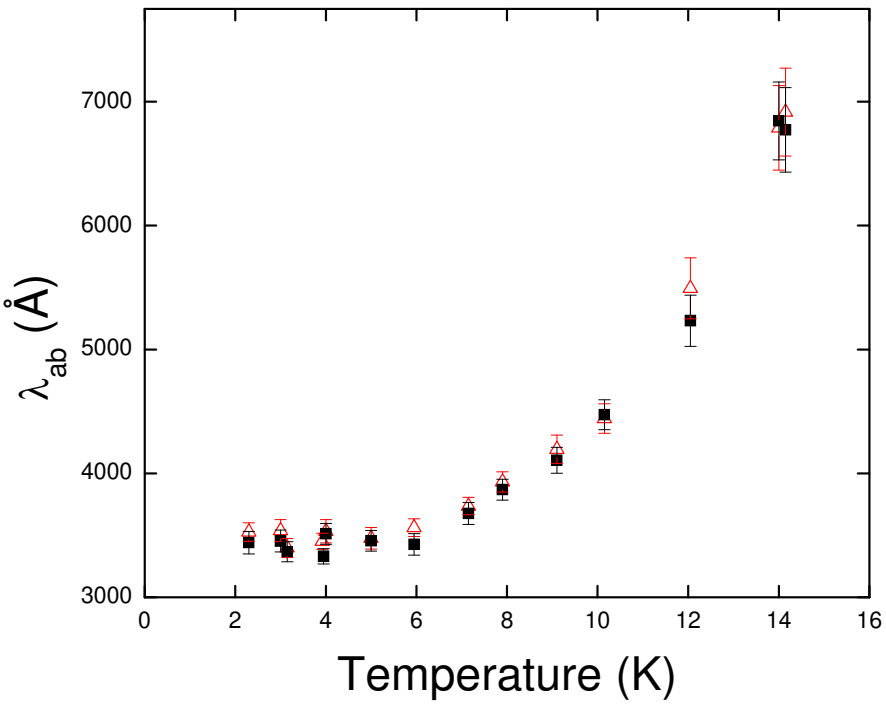

Fig. 5.10: Temperature dependence of λ_{ab} for a $Pr_{2-x}Ce_xCuO_4$ single crystal with ξ_{ab} = 30 Å (open triangles) and 60 Å (solid squares) at $H = 91$ Oe.

of ξ_{ab}. The value of $\lambda_{ab}(T)$ at any given temperature differs by less than 2% for the two values of ξ_{ab}. In the end, we fixed the value of ξ_{ab} at 60 Å, which is consistent with the value of the upper critical field $H_{c2} = \Phi_0/2\pi\xi_{ab}^2$ measured in Ref. [33].

Figure 5.11 shows the temperature dependence of $\lambda_{ab}^{-2}(T)$ at $H = 91$ Oe. The solid curve is a fit to the relation

$$\lambda_{ab}^{-2}(T) = \lambda_{ab}^{-2}(0)[1-(T/T_c)^2], \tag{5.5}$$

where $\lambda_{ab}(0) = 3369 \pm 73$ Å and $T_c = 15.9 \pm 0.2$ K. We note that the value of T_c is roughly equal to the temperature below which the dc bulk magnetic susceptibility flattens off under ZFC conditions (see Fig. 3.2).

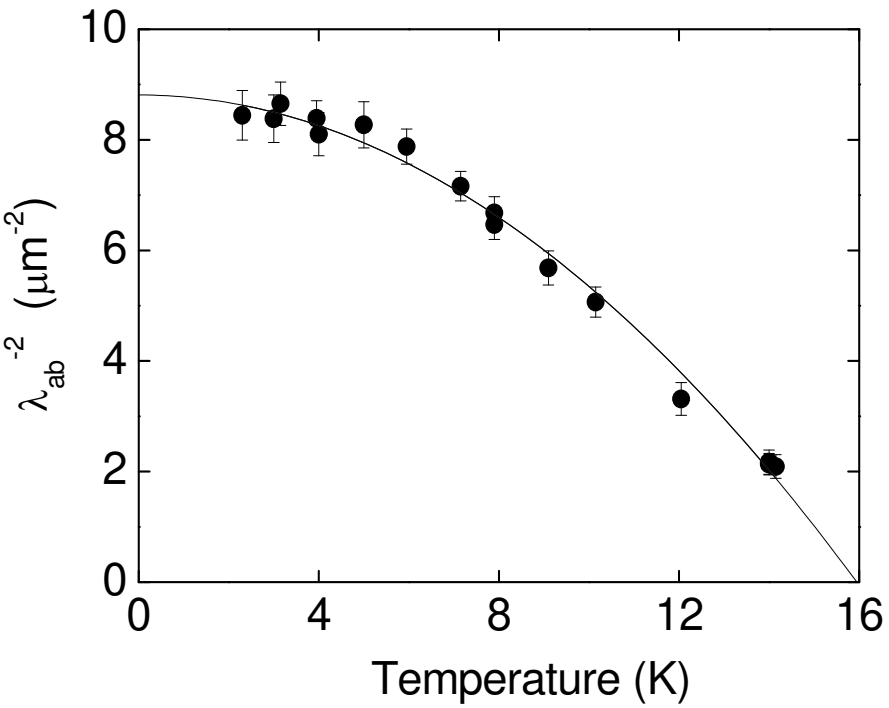

Fig. 5.11: Temperature dependence of the magnetic penetration depth $\lambda_{ab}^{-2}(T)$ at $H = 91$ Oe. The solid curve is fit of the data to Eq. (5.5).

Figure 5.12 shows the temperature dependence of $\lambda_{ab}(T)$ in a second $Pr_{2-x}Ce_xCuO_4$ single crystal at H = 200 Oe. The large error bars indicate that λ_{ab} is poorly determined due to the broadening effects with increased applied magnetic field described earlier.

Figure 5.13 shows the normalized magnetic penetration depth $\lambda_{ab}^{-2}(T)/\lambda_{ab}^{-2}(0)$ plotted as a function of the reduced temperature T/T_c at H = 91 Oe. Also shown are measurements in $La_{2-x}Sr_xCuO_4$ at H = 2 kOe [13] and $YBa_2Cu_3O_{6.95}$ at H = 5 kOe [34] from earlier μSR studies. The graph, which assumes a value of $\lambda_{ab}(0)$ = 3300 Å for $Pr_{2-x}Ce_xCuO_4$ shows reasonable agreement with the hole-doped cuprates at temperatures down to $T \sim 0.2\ T_c$. Unfortunately, the cryostat used for cooling the crystals was limited to $T \geq 2.3$ K. This prevented a precise determination of the low temperature limiting behaviour of $\lambda_{ab}^{-2}(T)$.

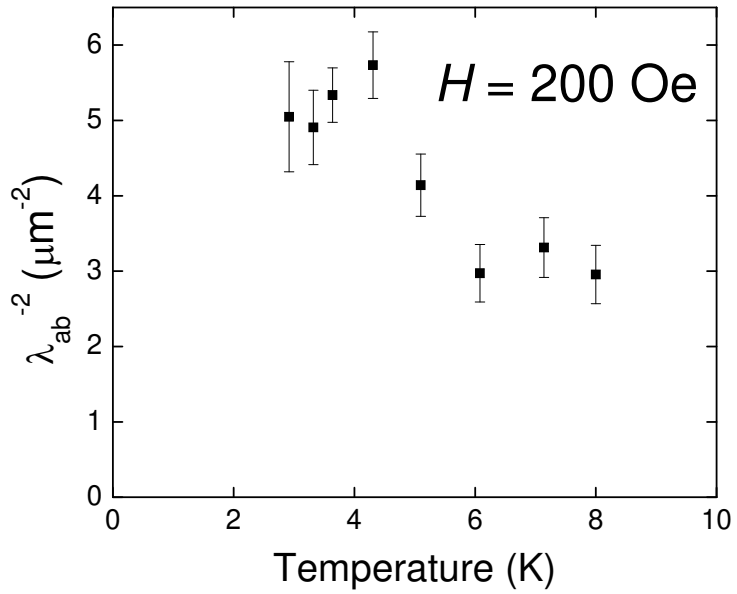

Fig. 5.12: Temperature dependence of the magnetic penetration depth in a second $Pr_{2-x}Ce_xCuO_4$ single crystal at H = 200 Oe.

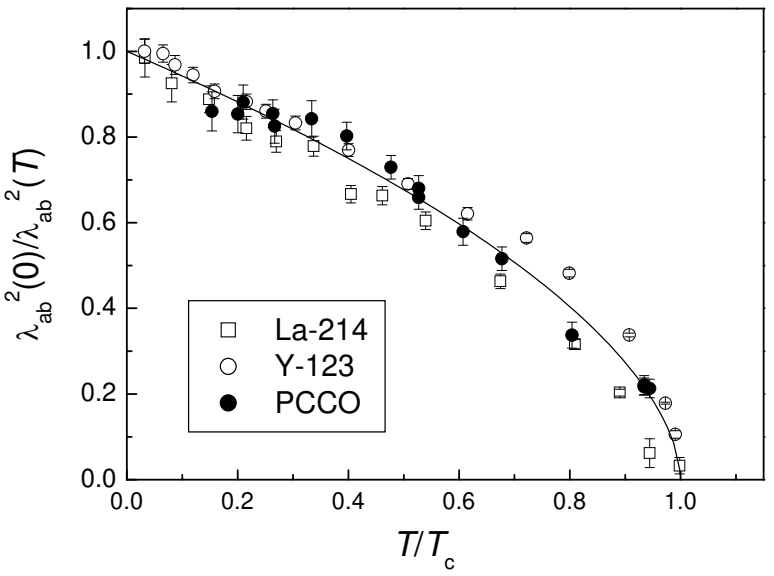

Fig. 5.13: Normalized magnetic penetration depth $\lambda_{ab}^2(0)/\lambda_{ab}^2(T)$ as a function of reduced temperature T/T_c for $Pr_{2-x}Ce_xCuO_4$ single crystals at H = 91 Oe, $La_{2-x}Sr_xCuO_4$ at H = 2 kOe and $YBa_2Cu_3O_{6.95}$ at H = 5 kOe. The solid curve is a guide for the eye.

Chapter 6

Discussion

As shown in this thesis, the μSR technique can be used to measure the internal magnetic field distribution in the vortex state of a type-II superconductor. Determination of the fundamental length scale λ_{ab} from μSR measurements, requires that some assumptions be made in the modeling procedure, including the geometry of the vortex lattice. The latter is often determined by neutron scattering, however, due to the unavailability of large samples, the geometry in $Pr_{2-x}Ce_xCuO_4$ is not known. Nevertheless, there is every reason to expect a hexagonal vortex lattice at the low applied magnetic fields used in this work, where the interactions between vortices is weak.

The spatial field profile of the vortex lattice that was assumed in the analysis of the TF-μSR data [*i.e.* Eq. (2.7)], agrees extremely well with the exact numerical solutions of the GL equations at low applied fields. Given that this model has been successful in describing the magnetic field distribution of the vortex lattice in hole-doped HTSCs and conventional superconductors, it is a reasonable starting that approximation for $Pr_{2-x}Ce_xCuO_4$. However, a rigourous test of the appropriateness of this model awaits future μSR work on other samples, at low temperatures and higher magnetic fields.

The main objective of this thesis was to study the temperature dependence of the in-plane magnetic penetration depth λ_{ab} in $Pr_{2-x}Ce_xCuO_4$, as the limiting low-temperature behaviour of λ_{ab} reflects the nature of the pairing symmetry of the superconducting carriers. Generally speaking, measurements of the magnetic penetration depth by μSR are best performed at high transverse magnetic field, where the density of vortices in the sample is large. In this case a more uniform vortex lattice is established, because the intervortex repulsion force is able to overcome the flux pinning forces exerted by sample defects. Furthermore, a higher number of muons stop close to the vortex cores, providing a greater sensitivity to the high-field cutoff in fits to the measured internal magnetic field distribution. However, the $Pr_{2-x}Ce_xCuO_4$ single crystals studied here appear to have a spread in local magnetic susceptibilities (likely due to spatial variations of charge doping) that results in an increased μSR line width with increasing applied magnetic field. At high applied magnetic field this additional broadening makes it is impossible to isolate the internal magnetic field distribution associated with the vortex lattice. Consequently, the present study of λ_{ab} in $Pr_{2-x}Ce_xCuO_4$ single crystals was restricted to low applied magnetic fields. Despite this limitation a considerable amount of effort was devoted to independently determining the value of the superconducting coherence length ξ_{ab}. Attempts were made to fit the μSR time spectrum at each temperature below T_c assuming a fixed value of ξ_{ab}. In particular, ξ_{ab} was determined as the value at which χ^2/NDF was minimized (where $NDF \equiv$ number of degrees of freedom). A similar approach was taken, where instead the value of the Ginzburg-Landau parameter κ_{ab} ($= \lambda_{ab}/\xi_{ab}$) was fixed in the fitting procedure. However, for both approaches, it was found that χ^2/NDF did not converge to a minimum at all temperatures, due to the insensitivity of the fits to the high-field cutoff. In the end, a reliable value of $\xi_{ab} = 60$ Å was used, which is consistent with reported values of H_{c2} in $Pr_{2-x}Ce_xCuO_4$. A

simple visual inspection of the fits in the frequency domain was also done to verify that this value was reasonable.

The temperature dependence of λ_{ab}^{-2} determined in $Pr_{2-x}Ce_xCuO_4$ above 0.2 T_c agrees with that determined previously by μSR in hole-doped HTSCs, although the uncertainty in the measurements is too large for a stringent comparison. A unique identification of the pairing symmetry in $Pr_{2-x}Ce_xCuO_4$ requires measurements of λ_{ab} at lower temperatures. Unfortunately, the small size of the $Pr_{2-x}Ce_xCuO_4$ single crystals that are currently available requires the use of a specialized low-background experimental setup. This arrangement is incompatible with a dilution refrigerator, so larger $Pr_{2-x}Ce_xCuO_4$ single crystals are needed to extend the present study to lower temperatures.

A surprising result in our study of superconducting $Pr_{2-x}Ce_xCuO_4$, was the observation of an enhanced average local magnetic field at the muon site (B_0) upon cooling the single crystals below T_c in a weak external magnetic field. Since the measurements of the bulk magnetic susceptibility exhibit the usual diamagnetic response characteristic of a superconductor, the increased local magnetic field must arise from the onset of spontaneous magnetic order. Although we calculate that such onset of magnetic ordering will reduce the initial asymmetry by ~ 19 % at the lowest temperature, this is not evident from the measurements for two reasons: First, the sample was mounted on a light guide which thermally contracts when it is cooled down. This introduced a systematic uncertainty in the initial asymmetry. Second and more importantly, the unusual situation of having the simultaneous onset of magnetic order and a vortex lattice makes it difficult to extract accurate values of the initial asymmetry across T_c, because the functional form of the internal magnetic field distribution dramatically changes.

From the dependence of B_0 on the external magnetic field H and dipolar field calcu-

lations, it appears that the enhanced local magnetic field detected by μSR arises from the onset of antiferromagnetic (AF) order of the Cu spins. In particular, the Cu-spin structure required to explain the μSR results is the noncollinear arrangement previously identified in non-superconducting $Pr_{2-x}Ce_xCuO_4$ by neutron scattering [30] and μSR [31]. A slight canting of the Cu spins out of the CuO_2 plane produces a dipolar magnetic field at the muon stopping site which is parallel to the basal plane. Since the muon detects the vector sum of local magnetic fields from different sources, the total average internal magnetic field that the muon senses in the presence of AF order exceeds the external field H.

Because μSR is sensitive to magnetic volume fractions, macroscopic phase separation would give rise to more than one distinct μSR signal. However, essentially all of the implanted muons see an increased local magnetic field below T_c, which is visually apparent in the FFTs of the muon-spin precession signals. Thus, one can conclude that the field-induced AF order occurs throughout much of the sample volume. Note the ZF-μSR measurements indicate that approximately 83% of the sample volume contains static Cu moments.

Recently, neutron scattering measurements of the hole-doped HTSC $La_{1.9}Sr_{0.1}CuO_4$ showed that a large (140 kOe) external field induces AF order in approximately 50% of the sample below T_c [29]. This neutron study followed several other experimental works that detected AF correlations only in the regions near the vortex cores [35]. The emergence of AF correlations in the vortex cores of HTSCs, where the superconducting order parameter is suppressed, is predicted by a number of theoretical models [36]. The results on $Pr_{2-x}Ce_xCuO_4$ and that of Ref. [29] indicate that the external magnetic field stabilizes AF order well beyond the vortex cores. It is somewhat remarkable that a weak external magnetic field of only 90 Oe results in long-range AF order in the superconducting state of $Pr_{2-x}Ce_xCuO_4$. This may be due to the close proximity of the AF and superconducting

phases in electron-doped cuprates (see Fig. 1.1), although sample inhomogeneity may also play an important role in extending the AF order into the regions between vortices.

Bibliography

[1] J.G. Bednorz and K.A. Müller, Z. Phys. B **64**, 189 (1986).

[2] G.M. Luke, L.P. Le, B.J. Sternlieb, Y.J. Uemura, J.H. Brewer, R. Kadono, R.F. Kiefl, S.R. Kreitzman, T.M. Riseman, C.E. Stronach, M.R. Davis, S. Uchida, H. Takagi, Y. Tokura, Y. Hidaka, T. Murakami, J. Gopalakrishnan, A.W. Sleight, M.A. Subramanian, E.A. Early, J.T. Markert, M.B. Maple and C.L. Seaman, Phys. Rev. B **42**, 7981 (1990).

[3] Y. Tokura, H. Takagi and S. Uchida, Nature **377**, 345 (1989).

[4] M. Brinkmann, T. Rex, H. Bach and K. Westerholt, Phys. Rev. Lett. **74**, 4927 (1995).

[5] M. Matsuda, Y. Endoh and Y. Hidaka, Physica C **179**, 347 (1991).

[6] Y. Dalichaouch, M.C. de Andrade and M.B. Maple, Physica C **218**, 309 (1993).

[7] T.J. Jackson, T.M. Riseman, E.M. Forgan, H. Glückler, T. Prokscha, E. Morenzoni, M. Pleines, Ch. Niedermayer, G. Schatz, H. Luetkens and J. Litterst, Phys. Rev. Lett. **84**, 4958 (2000).

[8] C.C. Tsuei and J.R. Kirtley, Phys. Rev. Lett. **85**, 182 (2000).

[9] N.P. Armitage, D. H. Lu, D.L. Feng, C. Kim, A. Damascelli, K.M. Shen, F. Ronning, Z.X. Shen, Y. Onose, Y. Taguchi and Y. Tokura, Phys. Rev. Lett. **86**, 1126 (2001).

[10] J.D. Kokales, P. Fournier, L.V. Mercaldo, V.V. Talanov, R.L. Greene and S.M. Anlage, Phys. Rev. Lett. **85**, 3696 (2001).

[11] J.A. Skinta, T.R. Lemberger, T. Greibe and M. Naito, Phys. Rev. Lett. **88**, 207003 (2002).

[12] L. Alff, S. Meyer, S. Kleefisch, U. Schoop, A. Marx, H. Sato, M. Naito and R. Gross, Phys. Rev. Lett. **83**, 2644 (1999).

[13] G.M. Luke, Y. Fudamoto, K. Kojima, M. Larkin, J. Merrin, B. Nachumi, Y.J. Uemura, J.E. Sonier, T. Ito, K. Oka, M.C. de Andrade, M.B. Maple and S. Uchida, Physica C **282-287**, 1465 (1997).

[14] J.R. Cooper, Phys. Rev. B **54**, R3753 (1996).

[15] S.L. Lee, S.H. Kilcoyne and R. Cywinski, editor, *Muon Science. Muons in Physics, Chemistry and Materials.* (Institute of Physics Publishing, Bristol, 1999).

[16] J.H. Brewer in *Encyclopedia of Applied Physics* edited by G.L. Trigg. (VCH, New York, 1994) Vol. 11, 23.

[17] L.B. Okun, *Weak Interactions of Elementary Particles.* translated by S. and M. Nikolic; translation edited by J. Bernstein. (Pergamon, Oxford, 1965).

[18] J.H. Brewer, Hyperfine Interact. **8**, 831 (1981).

[19] A. Yaouanc, P. Dalmas de Réotier and E.H. Brandt, Phys. Rev. B **55**, 11107 (1997).

[20] A. Schenck, *Muon Spin Rotation Spectroscopy: Principles and applications in solid state physics.* (Adam Hilger, Bristol, 1985).

[21] R. Kubo and T. Toyabe in *Magnetic Resonance and Relaxation* edited by R. Blinc. (North-Holland, Amsterdam, 1967), 810.

[22] A. Amato, Rev. Mod. Phys. **69**, 1119 (1997).

[23] J.L. Peng, Z.Y Li and R.L. Greene, Physica C **177**, 79 (1991).

[24] M. Brinkmann, T. Rex, H. Bach and K. Westerholt, J. Crystal Growth **163**, 369 (1996).

[25] P. Richard, G. Riou, S. Jandl, M. Poirier, P. Fournier, V. Nekvasil and M. Diviš, submitted to Physica C Proceedings.

[26] M. Fujita, T. Kubo, S. Kuroshima, T. Uefuji, K. Kawashima, K. Yamada, I. Watanabe, and K. Nagamine, Phys.Rev.B **67**, 014514 (2003).

[27] M. Sigrist and T.M. Rice, J. Phys. Soc. Jpn. **61**, 4283 (1992).

[28] R.L. Lichti, D.W. Cooke and C. Boekema, Phys. Rev. B. **43**, 1154 (1991).

[29] B. Lake, H.M. Rønnow, N.B. Christensen, G. Aeppli, K. Lefmann, D.F. McMorrow, P. Vorderwisch, P. Smeibidl, N. Mangkorntong, T. Sasagawa, M. Nohara, H. Takagi and T.E. Mason, Nature **415**, 299 (2002).

[30] I.W. Sumarlin, J.W. Lynn, T. Chattopadhyay, S.N. Barilo, D.I. Zhigunov and J.L. Peng, Phys. Rev. B **51**, 5824 (1995).

[31] J. Akimitsu, J. Amano, M. Yoshinari, M. Kokubun, T. Iwasaki, S. Okuma, N. Nishida, K. Nishiyama and N. Mori, Hyperfine Interact. **85**, 187 (1994).

[32] J.E. Sonier, J.H Brewer and R.F. Kiefl, Rev. Mod. Phys. **72**, 769 (2000).

[33] R.W. Hill, C. Proust, L. Taillefer, P. Fournier and R.L. Greene, Nature **414**, 711 (2001).

[34] J.E. Sonier, J.H. Brewer, R.F. Kiefl, G.D. Morris, R.I. Miller, D.A. Bonn, J. Chakhalian, R.H. Heffner, W.N. Hardy and R. Liang, Phys. Rev. Lett. **83**, 4156 (1999).

[35] D. Vaknin, J.L. Zarestky and L.L. Miller, Physica C, **329**, 109 (2000).

[36] S.C. Zhang, Science **275**, 1089 (1997).